

# Local rigidification and possible coacervation of the *Escherichia coli* DNA by cationic nylon-3 polymers

Yanyu Zhu,<sup>1</sup> Lei Liu,<sup>1</sup> Mainak Mustafi,<sup>1</sup> Leslie A. Rank,<sup>1</sup> Samuel H. Gellman,<sup>1</sup> and James C. Weisshaar<sup>1,\*</sup>

<sup>1</sup>Department of Chemistry, University of Wisconsin, Madison, Wisconsin

**ABSTRACT** Synthetic, cationic random nylon-3 polymers ( $\beta$ -peptides) show promise as inexpensive antimicrobial agents less susceptible to proteolysis than normal peptides. We have used superresolution, single-cell, time-lapse fluorescence microscopy to compare the effects on live *Escherichia coli* cells of four such polymers and the natural antimicrobial peptides LL-37 and cecropin A. The longer, densely charged monomethyl-cyclohexyl (MM-CH) copolymer and MM homopolymer rapidly traverse the outer membrane and the cytoplasmic membrane. Over the next  $\sim 5$  min, they locally rigidify the chromosomal DNA and slow the diffusive motion of ribosomal species to a degree comparable to LL-37. The shorter dimethyl-dimethylcyclopentyl (DM-DMCP) and dimethyl-dimethylcyclohexyl (DM-DMCH) copolymers, and cecropin A are significantly less effective at rigidifying DNA. Diffusion of the DNA-binding protein HU and of ribosomal species is hindered as well. The results suggest that charge density and contour length are important parameters governing these antimicrobial effects. The data corroborate a model in which agents having sufficient cationic charge distributed across molecular contour lengths comparable to local DNA-DNA interstrand spacings ( $\sim 6$  nm) form a dense network of multivalent, electrostatic “pseudo-cross-links” that cause the local rigidification. In addition, at times longer than  $\sim 30$  min, we observe that the MM-CH copolymer and the MM homopolymer (but not the other four agents) cause gradual coalescence of the two nucleoid lobes into a single dense lobe localized at one end of the cell. We speculate that this process involves coacervation of the DNA by the cationic polymer, and may be related to the liquid droplet coacervates observed in eukaryotic cells.

**SIGNIFICANCE** Certain sequence-random, synthetic cationic copolymers disrupt bacterial membranes, a mode of antibacterial action reminiscent of the action of natural antimicrobial peptides. We use single-cell fluorescence microscopy to directly compare the symptoms induced in *Escherichia coli* during the attack of several  $\beta$ -peptide polymers and the natural antimicrobial peptides LL-37 and cecropin A. Agents with sufficient contour length and positive-charge density locally dramatically attenuates the jiggling motion of the chromosomal DNA. The suggested mechanism is noncovalent, electrostatic cross-linking across nearby DNA stands. Once the membrane is breached, the bacterial cytoplasm with its preponderance of anionic biopolymers attracts a very high, damaging concentration of polycations. Such mechanistic studies may inform the design of new antimicrobial agents.

Submitted May 27, 2021, and accepted for publication October 26, 2021.

\*Correspondence: [weisshaar@chem.wisc.edu](mailto:weisshaar@chem.wisc.edu)

Yanyu Zhu's present address is Department of Bioengineering, Stanford University, Stanford, California 94305.

Lei Liu's present address is Department of Chemistry, University of Chicago, Chicago, Illinois 60637.

Mainak Mustafi's present address is Department of Biochemistry and Molecular Biophysics, Columbia University, New York, New York 10032.

Leslie A. Rank's present address is Johnson & Johnson Consumer Health, Skillman, New Jersey 08558.

Yanyu Zhu, Lei Liu, and Mainak Mustafi contributed equally to this work.

Editor: Antje Pokorny Almeida.

<https://doi.org/10.1016/j.bpj.2021.10.037>

© 2021 Biophysical Society.

## INTRODUCTION

Widespread infection by antibiotic-resistant bacteria necessitates the design and development of new antimicrobial agents that target resistant pathogens (1–3). Natural antimicrobial peptides (AMPs; also called host-defense peptides), part of the host innate immune system of plants and animals, are promising agents in this context. AMPs comprise an ancient class of short- and medium-sized polypeptides (typically <40 amino acids) that exhibit broad-spectrum antibacterial activity against both Gram-negative and Gram-positive bacteria (2). Most AMPs are amphipathic and highly cationic in physiological conditions. They are attracted to and permeabilize the negatively charged



membranes of bacteria but leave the zwitterionic eukaryotic membranes intact (2). Permeabilization of the bacterial outer membrane (OM) and cytoplasmic membrane (CM), with the concomitant loss of the proton motive force and critical small molecules, has long been recognized as a primary cause of AMP activity. However, mounting evidence suggests that some AMPs may kill bacteria via non-membrane-permeabilization mechanisms that disrupt specific intracellular processes (2,4–6).

Recently several groups have shown that membrane permeabilization leads to a massive influx of certain cationic AMPs into the bacterial cytoplasm. The threshold concentrations of bound peptide molecules per cell needed to kill bacteria varies from  $7 \times 10^6$  to  $2 \times 10^8$ , depending on the peptide and measuring method (1,6–8). We suggest that the preponderance of large, polyanionic species (chromosomal DNA, mRNA, rRNA, and ribosomes) renders the bacterial cytoplasm highly attractive to polycationic AMPs. Presumably the key driving force for AMP absorption is Coulombic attraction between polycations and polyanions enhanced by the entropically favorable concomitant release of small cations (mostly  $K^+$ ) to the cell surround (6).

We have used single-cell fluorescence microscopy to study the effects of AMPs on live *Escherichia coli* cells in real time (5,6,9,10). At concentrations comparable to the minimal inhibitory concentration (MIC), the human antimicrobial peptide LL-37 (+6 net charge,  $\sim 10.4$  nm in backbone contour length) permeabilizes both the OM and CM of *E. coli* to globular proteins and to smaller species on a timescale of several minutes (6). We estimated that on average each *E. coli* cell subsequently absorbs  $\sim 10^8$  LL-37 copies, corresponding to a mean concentration of  $\sim 90$  mM averaged over the entire cell volume (cell membranes, periplasm, and cytoplasm) (6).

We also tracked the motion of the DNA locus *Right 2* with 30-nm localization accuracy before and after CM permeabilization by LL-37 (6). The local jiggling motion of *Right 2* essentially freezes within 1 min of CM permeabilization. The chromosomal DNA meshwork has apparently rigidified, at least locally. We speculated that the high concentration of absorbed polycationic LL-37 forms a dense, fluctuating network of noncovalent, electrostatic “pseudo-cross-links” within the chromosomal DNA. In addition, single-particle tracking showed that the average diffusion coefficient of ribosomal species decreases by a factor of 2, whereas motion of a substantial subpopulation essentially halts. Some of the 70S-polysomes are frozen in place. The damage inflicted on bacterial cells by AMPs goes well beyond membrane permeabilization. The parallel occurrence of multiple damage pathways helps explain why bacteria develop resistance to AMPs very slowly.

Modifications of natural AMP sequences have been actively investigated for their potential use as antimicrobial agents. However, such  $\alpha$ -peptides suffer from the high cost of synthesis of a defined sequence and from susceptibil-

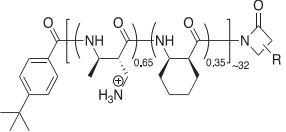
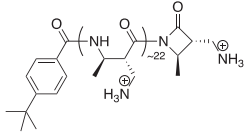
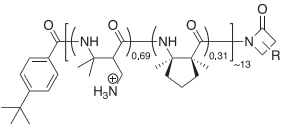
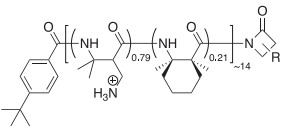
ity to proteolytic degradation. Substantial effort has been devoted to the development of synthetic analogs of natural AMPs that utilize different polymeric backbones. We have previously reported several sequence- and stereorandom nylon-3 polymers ( $\beta$ -peptide backbone) that mimic natural AMPs in antibacterial ability while minimizing hemolysis (11–15). Such sequence-random copolymers are much easier to synthesize than peptides, and they also resist proteolysis.

The primary purpose of this study is to test whether, like LL-37, the nylon-3 polymers can rigidify the chromosomal DNA and diminish ribosome mobility after penetration of the CM.

By testing polymers of varying composition and mean chain length, we can begin to understand what chemical and physical properties enable these effects. Typical DNA-DNA nearest interstrand distances in *E. coli* are  $\sim 6$  nm (16). We reasoned that the ideal pseudo-cross-linking agent should have sufficient backbone contour length to span at least a 6-nm gap and sufficient cationic charge density at both ends to enable strong electrostatic binding to DNA. Accordingly, we have studied two chemically well-defined AMPs (LL-37 and cecropin A) and four polymer mixtures with different charge densities and mean backbone contour lengths as described in Table 1. Our study mainly focuses on one of the polymers called MM-CH, which is copolymerized from monomethyl  $\beta$ -lactam (MM) and cyclohexyl  $\beta$ -lactam (CH) monomers, mixed in a 65:35 molar ratio. The MM subunit after deprotection has an ammonium group, which has a positive charge at the physiological pH. The CH subunit is hydrophobic. The results reveal the multipronged nature of the attack of MM-CH on *E. coli* and support formation of a dense meshwork of DNA-DNA pseudocrosslinks shortly after the polymer gains access to the cytoplasm. Cecropin A, similar to LL-37 in length and with the same +6 net charge, has its positive charges concentrated toward the N-terminus and is less effective in DNA rigidification. The two longest, most densely charged polymers (MM-CH and MM homopolymer) are comparable to LL-37 in their degree of DNA rigidification. The two shorter, densely charged polymers (dimethyl-dimethylcyclopentyl (DM-DMCP) and dimethyl-dimethylcyclohexyl (DM-DMCH)) are less effective. The rigidification of DNA and the cytoplasm greatly inhibits the essential motion of ribosomal species and of the DNA-binding protein HU.

For the MM-CH copolymer and MM homopolymer, at longer times ( $>30$  min) after the onset of polymer flow we discovered a surprising additional effect on the gross DNA morphology. In our relatively fast growth condition at  $30^\circ\text{C}$  (45 min doubling time), the chromosomal DNA normally exhibits two distinct, axially separate nucleoid lobes. We found that MM-CH copolymer and MM homopolymer can cause gradual coalescence of the two lobes into a single lobe of much higher apparent density localized at one end of the cell. The other four agents showed no such effect. We

**TABLE 1 Comparison of physical and chemical properties of AMPs and polymers**

Peptide/polymer <sup>a</sup>	Sequence/structure	Contour length <sup>b</sup>	Net charge	Net charge density	Rigidify DNA?	Coalesce DNA lobes?
MM-CH		11.5 nm	Avg +21	+1.83 e/nm	Strong	Yes
MM homopolymer		7.9 nm	Avg +22	+2.78 e/nm	Strong	Yes
LL-37	LLGDFFRKSKEKIG KEFKRIVQRIKDFL RNLVPRTES	10.4 nm	+6	+0.58 e/nm	Strong	No
Cecropin A	KWKLFFKKIEKVG QNIRDGIIKAGPAV AVVGGATQIAK	10.4 nm	+6	+0.58 e/nm	Less effective	No
DM-DMCP		4.7 nm	Avg +9	+1.91 e/nm	Less effective	No
DM-DMCH		5.0 nm	Avg +11	+2.2 e/nm	Less effective	No

<sup>a</sup>Naming convention specifies the side chains of the cationic and hydrophobic monomers used, with the cationic side chain first and the hydrophobic side chain second, separated by a hyphen.

<sup>b</sup>The contour length is estimated by multiplying N-to-N spatial distance by the degree of polymerization. The N-to-N spatial distance between two neighboring residues was measured with PyMol based on the crystal structures of poly- $\alpha$  and poly- $\beta$ -peptides. The length of the end groups are neglected. The relative lengths between species can be compared. The actual end-to-end distance of the polymer will generally be shorter than the counterlength reported here. For example, we estimated LL-37 has a length of 5.7 nm in an  $\alpha$ -helix conformation.

speculate that this new effect may be related to the well-known polymer phenomenon of coacervation, the condensation of DNA in solution phase by a sufficient concentration of a sufficiently long positively charged polymer (17–20).

## MATERIALS AND METHODS

Nylon-3 polymers were prepared in a nitrogen-purged glove box at room temperature using previously reported methods (13). Live *E. coli* cells are immobilized on a polylysine-coated coverslip in a microfluidic channel that enables us to begin flowing the antimicrobial agent at known concentration at time  $t = 0$ . An EMCCD camera images the cells in real time. The strains described in Table S2 enable fluorescence imaging of green fluorescent protein (GFP) that has been exported to the periplasm; of ribosomal species labeled by the photoswitchable protein S2-mEos2 or S2-Dendra2; of the DNA locus *Right2* labeled by ParB-GFP binding to an engineer *parS* site; or of the global distribution of chromosomal DNA labeled by the dye Sytox Orange or by the nonspecific DNA-binding protein HU-PAM-Cherry. Additional details are provided in each subsection of Results and in the Supporting materials and methods.

## RESULTS

### Osmotic effects and CM permeabilization by MM-CH copolymer

The MIC results for the different polymers and AMPs against different bacterial strains are shown in Table 2. Throughout this study, beginning at time  $t = 0$ , we flow  $2 \times$  MIC of each agent to ensure that the vast majority of the bacterial cells are affected by the antimicrobial agent on the imaging timescale of 30–90 min. First we carried out a detailed study of the effects of copolymer MM-CH on *E. coli* using the strain JCW10 that expresses GFP from a plasmid and exports it to the periplasm (Table S2, WT-ppGFP) (11). We included 5 nM Sytox Orange in the flowing medium.

For these 90-min long, three-channel experiments, in each 12-s cycle, we interleave a phase contrast image (enabling measurement of tip-to-tip cell length), a GFP

**TABLE 2** MIC for different bacterial strains with different agents

Agent	VH1000	JCW154	MSG192	MG1655	JCW10	SM7	MDG196
MM-CH copolymer ( $\mu\text{g/mL}$ )	25	25	25	25	25	25	25
MM homopolymer ( $\mu\text{g/mL}$ )	31	31	31	31	31	31	31
LL-37 ( $\mu\text{M}$ )	4	4	4	4	4	4	4
Cecropin A ( $\mu\text{M}$ )	2	2	2	2	2	2	2
DM-DMCP copolymer ( $\mu\text{g/mL}$ )	12.5	12.5	12.5	12.5	12.5	–	–
DM-DMCH copolymer ( $\mu\text{g/mL}$ )	12.5	12.5	12.5	12.5	12.5	–	–

Note that MIC is measured in  $\mu\text{M}$  for the two chemically defined AMPs, but in  $\mu\text{g/mL}$  for the polymers, which lack a well-defined molecular weight. From the known molecular weights of the natural AMPs, for LL-37 we can convert  $\text{MIC} = 4 \mu\text{M} = 18 \mu\text{g/mL}$ ; for cecropin A,  $\text{MIC} = 2 \mu\text{M} = 8 \mu\text{g/mL}$ . When expressed in  $\mu\text{g/mL}$ , all the MIC values lie in a fairly narrow range from 8 to 31  $\mu\text{g/mL}$ .

image (providing total GFP fluorescence intensity and GFP spatial distribution), and a Sytox Orange image (determining when the dye gains access to the cytoplasm and binds to the chromosomal DNA to become fluorescent).

Results for a representative cell (Video S1) are shown in Fig. 1, A–C. Before flowing MM-CH at the concentration of 50  $\mu\text{g/mL}$  (image at  $t = -4$  min), the GFP channel shows the characteristic periplasmic “halo” distribution (Fig. 1, A and B). Within one 12-s camera frame of the onset of flow, the apparent cell length begins to shrink. Several minutes later it partially recovers, as observed before (11). Until  $t = 2.2$  min, the periplasmic GFP gradually accumu-

lates at the two cell endcaps (Fig. 1, A and B). We interpret this as an osmotic effect known as “plasmolysis” (21). A large concentration of highly cationic MM-CH along with its counterions has translocated across the OM to the periplasm, leading to an apparent osmotic upshift that draws water from the cytoplasm to the periplasm. To accommodate the cytoplasmic volume decrease and to conserve the surface area of the CM, the CM collapses its endcaps and creates more periplasmic volume at the two cell poles, between the CM and OM. The periplasmic GFP redistributes to the cell poles (Fig. 1, A and B). A more detailed explanation can be found in (11). At this stage, the periplasmic GFP

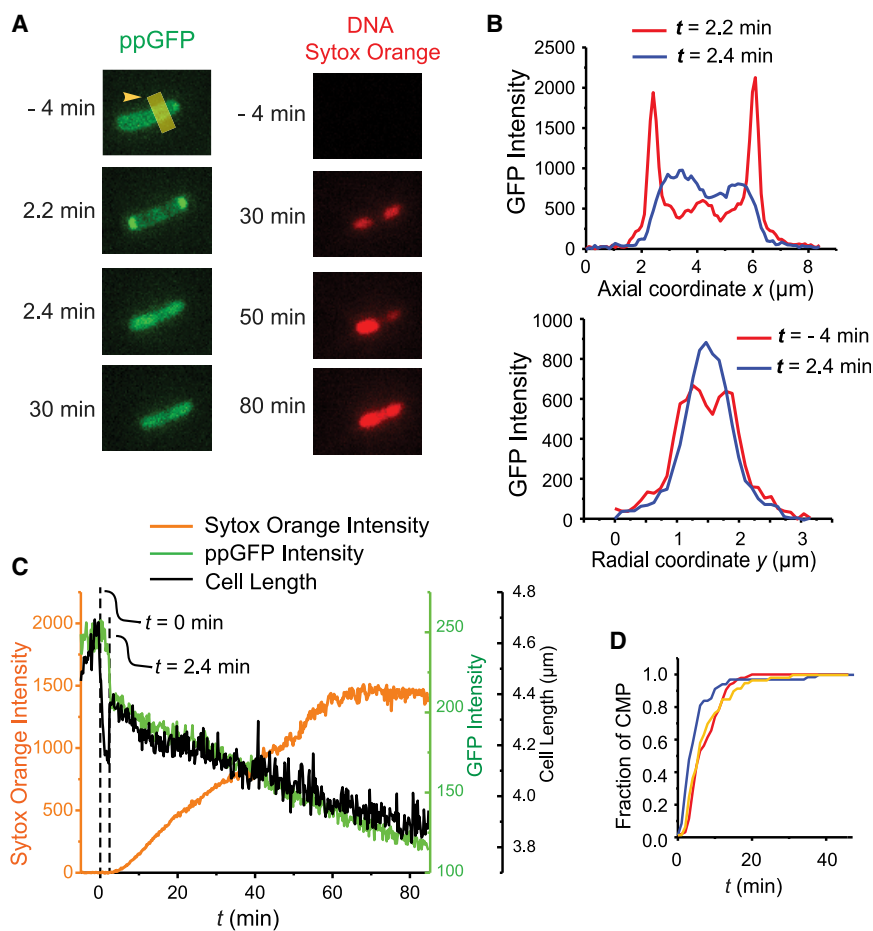


**FIGURE 1** Effects of copolymer MM-CH on a representative *E. coli* cell that exports GFP to the periplasm (Video S1). Flow of  $2\times$  MIC of MM-CH in EZRDM with 5 nM of the DNA stain Sytox Orange begins at  $t = 0$ . Images acquired at 12 s per frame. (A) Fluorescence snapshots of GFP (left) and Sytox Orange (right). (B) Projected axial (top) and transverse (bottom) GFP intensity profiles at the times indicated. (C) Cell length (black), total GFP intensity (green) and Sytox Orange intensity (orange) versus time. Note: scales for GFP intensity and cell length are very different. Over the time interval  $t = 2$ –60 min, GFP intensity decreases by 50%, but cell length decreases by only 11%. (D) Cumulative distribution function of the fraction of cells for which CM permeabilization has occurred versus time for LL-37, MM-CH copolymer, and MM homopolymer, each at  $2\times$  MIC.

has not leaked into the surroundings, indicating that MM-CH has traversed the OM without permeabilizing it to GFP.

From  $t = 2.2$  to  $2.4$  min, the total GFP intensity decreases by  $\sim 20\%$ ; this loss of GFP intensity indicates that the OM has become permeabilized to GFP. The apparent cell length partially recovers, probably due to the initial osmoprotection response of the cell (active import of  $K^+$ ) (11). At  $t = 2.4$  min the CM becomes permeabilized to GFP and the GFP intensity pattern abruptly changes to that of a filled cytoplasm (Fig. 1, A and B). The rate of loss of total GFP intensity decreases. Evidently either the OM or the CM or both membranes quickly reseal(s), much as observed earlier for melittin (10).

From  $t = 2.4$  to 85 min, GFP intensity gradually decreases by  $\sim 50\%$ . This decrease is due in part to photobleaching. At these longer times, we infer that the cell envelope is nearly impermeable to GFP and other such globular proteins. The behavior described here is quite general. Across several experiments, all 37 cells that successfully expressed GFP exhibited similar behavior.

Sytox Orange intensity starts to increase at  $t = 3$  min for this cell, then increases almost linearly for  $\sim 60$  min and finally levels off from 60 to 80 min, likely due to saturation of the available DNA-binding sites. Both OM and CM have become permeable to the small dye molecule and remain so even after the transient events of high permeability to GFP. Over the same 80-min time window, cell length gradually decreases by  $\sim 11\%$ . This may be due to gradual loss of small osmolytes and a corresponding decrease in cytoplasmic osmolality. We define the onset of Sytox Orange intensity as the time of CM permeabilization (CMP; Table 3). In Fig. 1 D, we compare the cumulative distribution function of CMP times for MM-CH, MM homopolymer, and LL-37. In all three cases, essentially all cells have had their CM permeabilized within 25 min after treatment begins. The MM homopolymer permeabilizes the CM slightly more slowly than MM-CH, perhaps because it lacks the hydrophobic CH subunit.

### Local rigidification of the chromosomal DNA by MM-CH

To characterize the local dynamics of chromosomal DNA before and after MM-CH treatment, we tracked the DNA locus *Right 2* labeled by the fusion protein ParB-GFP (strain JCW154, Table S2). In this strain, the fluorescent ParB-GFP protein expressed from a plasmid polymerizes specifically at the *parS* site engineered into the chromosome

near the locus *Right 2* (22). The resulting bright puncta can be tracked for some 600 frames with an exposure time of 50 ms/frame without extensive photobleaching. For comparison, we also include the results for normally growing cells (6), growing cells treated with carbonylcyanide-*m*-chlorophenylhydrazone (CCCP) + 2-deoxyglucose (which depletes ATP by the dissipation of the proton motive force and prevention of glycolysis) (23), and cells after chemical fixation by formaldehyde (6).

At 1 s/frame, we can monitor locus position with  $\sim 30$  nm accuracy for 600 frames = 10 min. We first calculate the mean-square displacement (MSD) averaged over trajectories obtained within different 10-min time windows after the onset of MM-CH flow. For each time window, we estimate an apparent diffusion coefficient  $D_{app}$  from the slope of the linear least-squares fit to the first 10 experimental points of the MSD plot. A plot of  $D_{app}$  versus the central time for each window gives a sense of the gradual slowing of the DNA local jiggling motion over time (Fig. S1). For example, the MM-CH curve shows that the copolymer attenuates the DNA loci motion by more than a factor of 10 over 45 min (from  $D_{app} = 2.0 \times 10^{-4}$  to  $1.7 \times 10^{-5} \mu\text{m}^2/\text{s}$ ), and that most of the attenuation occurs over the first 10 min (Table 3). In addition, all of the polymers and AMPs permeabilize the CM of most cells within 25 min. We designate cells 25 min after injection of the antibacterial agent as “polymer- or AMP-treated cells.” Rigidification of the DNA occurs on the same timescale as CM permeabilization (Figs. 1 D and S1). This is consistent with our earlier study of LL-37, in which the freezing of DNA loci motion occurred within 1 min of the time of CM permeabilization ((6); Fig. 1 D).

By combining data at times greater than 25 min from all the trajectories including all experiments, for each agent we calculate the final MSD plot after treatment (Fig. 2, A and B). These MSD plots show clear negative curvature for treated cells as well as for normally growing cells (6,24). Such curvature is the signature of subdiffusive motion, as expected for the local dynamics of a small segment within a large, confined polymer. The degree of curvature is less for the agents that cause the greatest attenuation of DNA motion. To enable semiquantitative comparisons on the 10-s timescale, for each MSD curve we compute an apparent diffusion coefficient  $D_{app}$  from the slope of the linear least-squares fit to the first 10 experimental points. Numerical results (Table 4) are:  $D_{app} = (2.0 \pm 0.2) \times 10^{-4} \mu\text{m}^2/\text{s}$  for normal growing cells;  $(4.6 \pm 0.2) \times 10^{-5} \mu\text{m}^2/\text{s}$  for cells after CCCP treatment;  $(7.6 \pm 2.1) \times 10^{-6} \mu\text{m}^2/\text{s}$  for fixed cells;  $(1.7 \pm 0.1) \times 10^{-5} \mu\text{m}^2/\text{s}$  for cells 25 min after treating MM-CH.

**TABLE 3** Timing and extent of CM permeabilization

Cell treatment	Fraction of cells permeabilized within 1 h	Mean time to CM permeabilization (min)
MM-CH copolymer	100%	$6.8 \pm 6.2$
MM homopolymer	98.3%	$8.3 \pm 5.9$
LL-37	100%	$8.2 \pm 4.3$

### Attenuation of ribosome and HU diffusion by MM-CH

To further explore the effect of MM-CH on cytoplasm, we tracked the diffusive motion of single fluorescently labeled

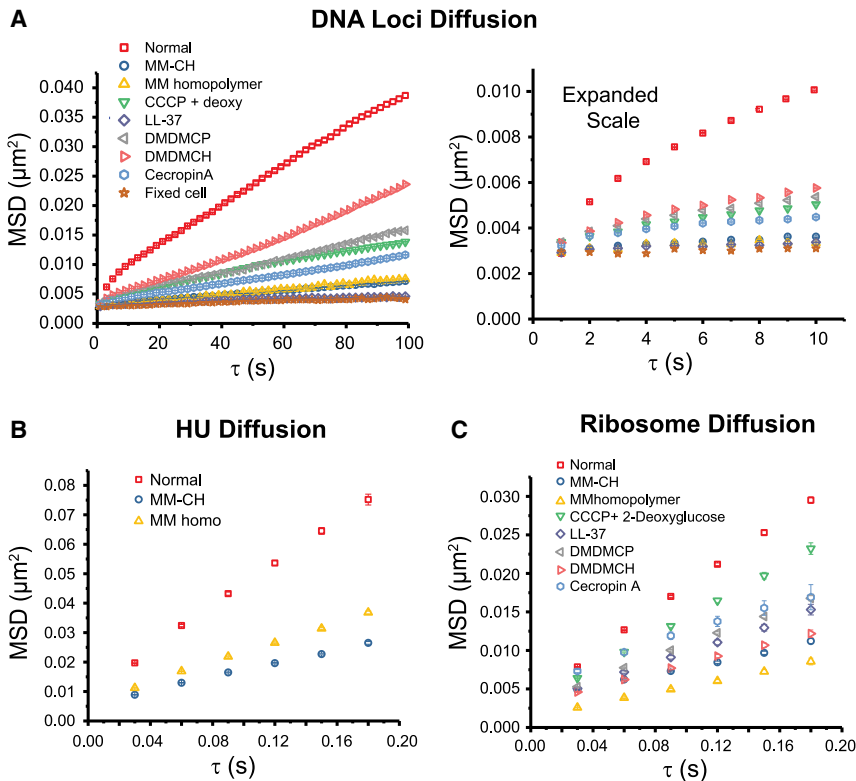


**FIGURE 2** Effect of AMPs and polymers on DNA and protein diffusive motion. (A) MSD versus lag time for DNA loci under various treatments, obtained from videos taken at 1 s/camera frame for 600 frames. Data for treated cells obtained at least 25 min after beginning of flow of antimicrobial agent. Left: MSD covering 100 s. Right: expanded view of the first 10 s. Apparent diffusion coefficient  $D_{app}$  obtained from linear fit to first 10 points. Numerical results are in Table 4. (B) HU-PAmCherry MSD versus lag time with trajectories taken at 30 ms/frame in normal growth and after polymer. The apparent diffusion coefficient  $D_{app}$  is obtained by linear fitting of the first three data points. The numerical results are:  $(0.098 \pm 0.004) \mu\text{m}^2/\text{s}$  for cells in normal growth (data from (24));  $(0.034 \pm 0.001) \mu\text{m}^2/\text{s}$  for cells after MM-CH;  $(0.045 \pm 0.002) \mu\text{m}^2/\text{s}$  for cells after MM homopolymer. (C) Ribosome MSD versus lag time from S2-mEos2 trajectories taken at 30 ms/frame in after the different treatments as shown. The apparent diffusion coefficient  $D_{app}$  is obtained by linear fitting of the first three data points. Numerical results are in Table 4.

ribosomal particles before and after polymer treatment at 30 ms/frame. These experiments use the strain MDG196, in which the chromosomal DNA is altered to append a photoconvertible mEos2 protein to the C-terminus of the ribosomal protein S2 (Table S2). In effect, we are tracking 30S ribosomal subunits, which may occur as either free 30S subunits or 30S subunits incorporated into translating 70S ribosomes, including 70S-polysomes.

We analyzed only those trajectories that last six steps or longer and truncated the longer trajectories at six steps. In Fig. 2 C, we compare MSD plots for ribosomes (S2-mEos2) in different conditions. The apparent diffusion coefficient  $D_{app}$  is obtained by linear fitting of the first three data

points. The numerical results (Table 4) are:  $(0.042 \pm 0.001) \mu\text{m}^2\text{-s}^{-1}$  for cells in normal growth;  $(0.028 \pm 0.001) \mu\text{m}^2\text{-s}^{-1}$  for cells after CCCP treatment (6);  $(0.010 \pm 0.001) \mu\text{m}^2\text{-s}^{-1}$  for cells after MM-CH treatment. MM-CH treatment diminishes the motion of ribosomal particles by a factor of 4. A separate experiment tracking the ribosomal protein S2-Dendra2 showed similar results (Fig. S2).

In the gated diffusion model of Chow and Skolnick (16), motion of the nonspecific DNA-binding protein HU would provide another probe of local DNA dynamics. We tracked single copies of HU-PAmCherry in the strain SM7. MSD plots for HU after MM-CH treatment are quite linear on a 180-ms timescale (Fig. 2 B). In this case, we estimate an apparent diffusion coefficient from the slope of the linear least-squares fit to the first three experimental points. The numerical results are  $D_{app} = (0.098 \pm 0.004) \mu\text{m}^2/\text{s}$  in normal growth conditions;  $(0.034 \pm 0.001) \mu\text{m}^2\text{-s}^{-1}$  for cells after MM-CH;  $(0.045 \pm 0.002) \mu\text{m}^2\text{-s}^{-1}$  for cells after MM homopolymer. MM-CH and MM homopolymer have a similar effect as LL-37 (6) in reducing the mean HU diffusion coefficient.

### Coalescence of two nucleoid lobes induced by MM-CH at long times

In the initial experiments incorporating Sytox Orange into the flow, we sometimes noticed a surprising change in the intensity distribution between the two nucleoid lobes at longer times. To more incisively explore the effects of

**TABLE 4** Apparent diffusion coefficients of DNA loci and ribosomal species after 25 min of polymer or peptide treatment

Cell treatment	$D_{app}$ ( $\mu\text{m}^2/\text{s}$ ) for DNA loci (1 s/frame)	$D_{app}$ ( $\mu\text{m}^2/\text{s}$ ) for ribosomal species (30 ms/frame)
Normal growth <sup>a</sup>	$(2.0 \pm 0.2) \times 10^{-4}$	$0.042 \pm 0.001$
CCCP + 2-deoxyglucose <sup>a</sup>	$(4.6 \pm 0.2) \times 10^{-5}$	$0.028 \pm 0.001$
Fixed cells <sup>a</sup>	$(7.6 \pm 2.1) \times 10^{-6}$	–
MM-CH	$(1.7 \pm 0.1) \times 10^{-5}$	$0.010 \pm 0.001$
MM homopolymer	$(1.2 \pm 0.3) \times 10^{-5}$	$0.0099 \pm 0.0004$
LL-37	$(1.0 \pm 0.1) \times 10^{-5}$	$0.018 \pm 0.001$
Cecropin A	$(3.1 \pm 0.4) \times 10^{-5}$	$0.023 \pm 0.001$
DM-DMCP	$(5.2 \pm 0.4) \times 10^{-5}$	$0.020 \pm 0.001$
DM-DMCH	$(6.3 \pm 0.4) \times 10^{-5}$	$0.013 \pm 0.001$

From slope of MSD plots. See text for additional information.

<sup>a</sup>Data from (6) included here for comparison.

MM-CH on nucleoid morphology, we conducted a set of experiments in which cells were prestained with 500 nM Sytox Orange for 10 min before imaging (25) and Sytox Orange was omitted from the flow. In these experiments, the total Sytox Orange fluorescence intensity inside each cell is approximately constant during the time of imaging. As before,  $2\times$  MIC of MM-CH flowed beginning at  $t = 0$ . Images of Sytox Orange fluorescence were acquired at 1 min per frame to minimize photobleaching over 90 min.

Sytox Orange fluorescence snapshots of a representative *E. coli* cell during the attack of MM-CH are shown in Fig. 3 A. Sytox Orange integrated intensity versus time for the entire cell and for the two individual lobes labeled *a*

and *b* are shown in Fig. 3 B. The total intensity within the cell remains almost constant during the  $\sim 1.5$  h of imaging. However, at  $t_1 = 26$  min the left nucleoid lobe *a* begins to merge into the right nucleoid lobe *b*, as shown by the decrease in intensity in region *a* and the simultaneous increase in intensity in region *b*. We denote this time  $t_1$  to mark the beginning of phase 1, coalescence of the two nucleoid lobes. This process continued until the combined nucleoid reached its most compact state at  $t_2 = 39$  min for this cell (the beginning of phase 2). The nucleoid remained in this compact state for  $\sim 20$  min, then began to expand at  $t_3 = 57$  min (the beginning of phase 3). The left nucleoid lobe intensity continues to increase until the final state is

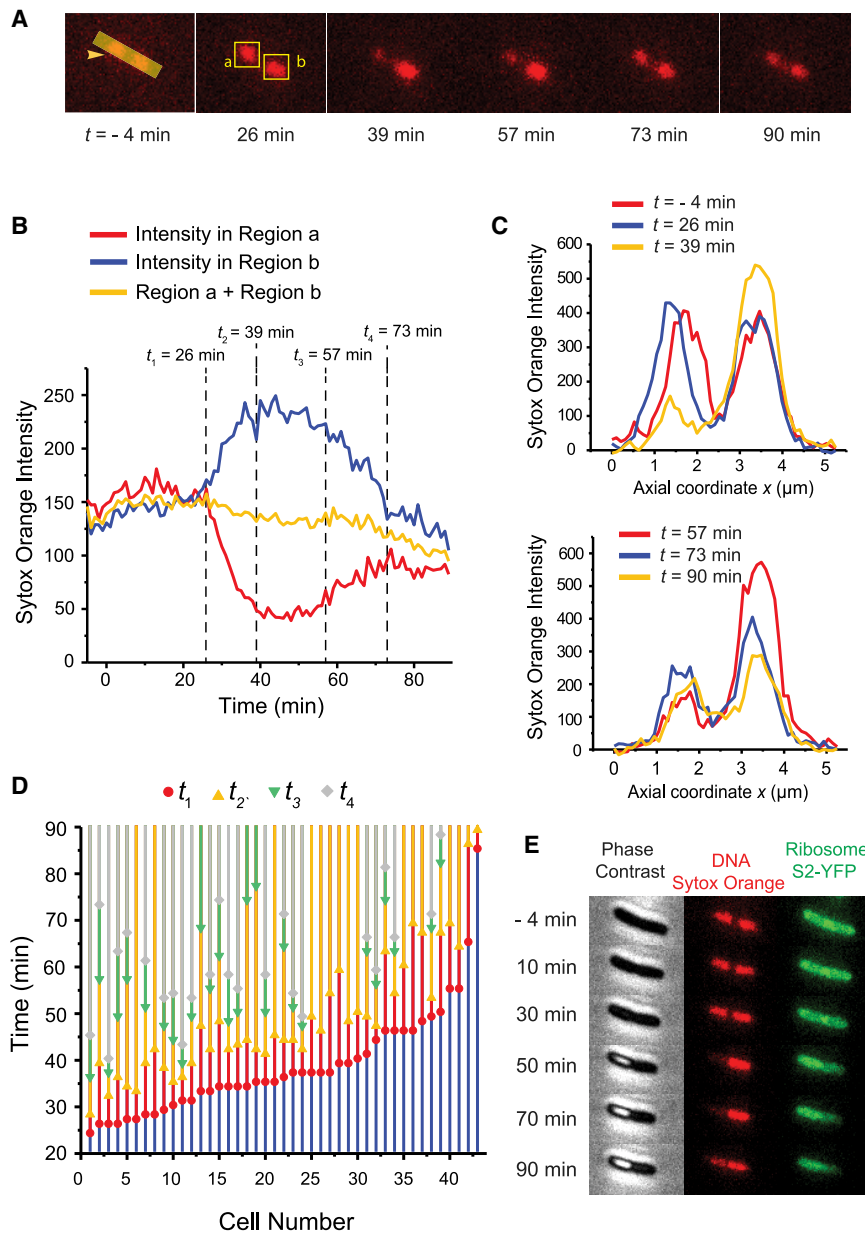


FIGURE 3 Effects of MM-CH on nucleoid morphology at long times. Chromosomal DNA was stained with 500 nM Sytox Orange for 10 min before imaging. Flow of  $2\times$  MIC MM-CH began at  $t = 0$ . Images acquired at 1 min per frame. (A) Sytox Orange fluorescence snapshots of single *E. coli* cell at different times. (B) Sytox Orange intensity versus time for the same cell shown in (A). Total Sytox Orange intensity from the entire cell (yellow curve), from the left nucleoid lobe (red curve, region *a* as in A), and from the right nucleoid lobe (blue curve, region *b* as in A). Total intensity from the entire cell is scaled by a factor of 1.6. Labeled times are  $t_1$  (beginning of coalescence of nucleoid lobes),  $t_2$  (beginning of phase 2, the nucleoid reaches its most compact state),  $t_3$  (beginning of phase 3, partial recovery), and  $t_4$  (nucleoids have reached the apparent final state). (C) Projected axial Sytox Orange intensity profile along the cell long axis (arrowhead in A) at different times. Left nucleoid lobe merged to the other one and partially recovered at later times. (D) The timeline of events  $t_1$ – $t_4$  for 43 cells from four experiments. (E) Phase contrast, Sytox Orange fluorescence and ribosome S2-YFP snapshots of single *E. coli* cell at different times after flowing MM-CH.

reached at  $t_4 = 73$  min (beginning of phase 4). This final detected stage is slightly different from the initial stage in that the intensity of lobe *a* remains somewhat lower than the intensity of lobe *b*. The projected axial Sytox Orange intensity profile along the cell long axis at different times is shown in Fig. 3 C.

We observed 61 cells from four different experiments; 43 cells showed a similar slow nucleoid coalescence/expansion phenomenon. The timeline of events  $t_1$  through  $t_4$  for these 43 cells is shown in Fig. 3 D. The cells exhibit strong heterogeneity in the occurrence and timing of different events.

For most cells, the coalescence begins  $\sim 30$  min after flowing MM-CH, much later than the osmotic effect and the membrane disruption events described above. Not all cells exhibit phase 3 and phase 4 during our 90-min imaging timescale. In phase 2, the diminished nucleoid lobe retains some residual intensity for some cells, as in Fig. 3 A, whereas for other cells, it completely disappears.

In phase 4, the diminished nucleoid lobe recovers to different degrees compared with the other lobe. An additional 18 cells from the four experiments did not exhibit such a nucleoid morphology change.

The analysis includes cells of all lengths. Both the cells undergoing DNA coalescence and cells not undergoing DNA coalescence include both septating cells and nonseptating cells of different lengths.

We repeated this experiment using the bacterial strain MSG192, in which the ribosomal protein S2 is labeled with YFP. We found that when the DNA lobes merged at one end of the cell, the ribosomes moved to the other end of the cell, where the DNA has become much less dense (Fig. 3 E, Video S2). The strong anticorrelation of the DNA and the ribosome spatial distributions that occurs in normal growth persists after the coalescence. Details are provided in Supporting materials and methods and Fig. S3.

We also carried out superresolution imaging of the nonspecific DNA-binding protein HU-PAMCherry. The results (Fig. S4) corroborate the widefield Sytox Orange results showing coalescence of the two nucleoid lobes at longer times for many cells. At  $t = 25$  min after MM-CH addition, for cells in the length range 4.0–4.3  $\mu\text{m}$ , we observed 17 cells showing two symmetric nucleoid lobes and 22 cells showing asymmetric nucleoid lobes. In addition, the superresolution HU-PAMCherry images enable us to compare the nucleoid radius of untreated cells with that of cells treated with 2X MIC MM-CH for 25 min, as described earlier (24). Details are provided in Supporting materials and methods.

For untreated cells,  $\langle r_{\text{nucleoid}} \rangle = 0.29 \pm 0.04 \mu\text{m}$  (33 cells with cell length in the range 4.0–4.3  $\mu\text{m}$ ) compared with  $\langle r_{\text{nucleoid}} \rangle = 0.22 \pm 0.05 \mu\text{m}$  (17 cells with two nucleoid lobes and cell length in the range 4.0–4.3  $\mu\text{m}$ ) for cells after treatment with MM-CH. Nucleoid lengths are similar under both conditions. The apparent nucleoid volume has shrunk by a factor of  $\sim 1.7$  (the square of the ra-

tio of radii) due to MM-CH treatment (Fig. S5). This may be a signature of coacervation, as discussed below.

### Upper limit on the total number of charges that MM-CH brings into the cell

One of the most important parameters in the coacervation of polymer mixtures is the ratio of the total concentration of positive charges on the polycations to the total concentration of negative charges on the polyanions (18,19,26). Global DNA rigidification by electrostatic cross-linking also requires adsorption of a large number of polycationic molecules. To explore the plausibility of coacervation as well as rigidification of DNA by MM-CH, we estimate an upper limit on the amount of MM-CH per bacterial cell using a similar method as reported before (6–8). We incubated various concentrations of MM-CH polymer with various total cell counts (colony-forming units, CFU per mL) in PBS solution for 60 min in the test tube. Then we aliquoted each sample into 96-well plates supplied with EZ rich, defined medium (EZRD) and incubated for 24 h. For each MM-CH concentration and for each initial cell count, we measured the optical density (OD) at 595 nm before and after 24-hr incubation of the cells with MM-CH. The change in optical density is defined as  $\Delta\text{OD} = \text{OD}_{t=24\text{ h}} - \text{OD}_{t=0}$ .

If the OD does not increase for 24-h, then that amount of MM-CH was large enough to kill the initial number of cells. In this way, we can measure the minimal bulk MM-CH concentration required to kill a particular initial number of cells. For example, the MM-CH concentration of 50  $\mu\text{g}/\text{mL}$  (as used in the flow experiments) is sufficient to kill  $4 \times 10^7$  CFU/mL (Fig. S6). If it were the case that all of the MM-CH were absorbed by the bacterial cells, then on average each cell would have absorbed  $\sim 2.6 \times 10^9$  positive charges. Because some of the MM-CH may remain in solution under these conditions, this number provides an upper bound to the actual number of positive charges absorbed. Details of the calculation are provided in Supporting materials and methods.

In the earlier work on LL-37, we used fluorescence and GC/MS to measure the fraction of LL-37 bound to the cells. For a bulk concentration of 20  $\mu\text{M}$ , we estimated that an average of  $\sim 2 \times 10^8$  LL-37 copies were absorbed per cell. Net positive charge of LL-37 at neutral pH is +6, so the net positive charge absorbed per cell was  $\sim 1.2 \times 10^9$ , comparable with the estimated upper bound on MM-CH uptake.

### Recovery experiments

To explore whether or not the short-term DNA rigidification and longer-term DNA coalescence are related to bacterial growth inhibition, we conducted a series of recovery experiments. In these experiments, we flow 2X MIC of MM-CH in EZRD across plated WT cells for 5 or 10 min and then



change the flow to EZRDM without MM-CH for an additional 90 min. Phase contrast imaging provides an estimate of cell length versus time to test for possible recovery of cell growth. We observed 37 cells after 5-min exposure to MM-CH and 26 cells after 10-min exposure. In all 63 cases, the brief exposure was sufficient to completely halt apparent cell growth for at least 90 min of observation time by phase contrast imaging. However, for 5-min exposure to MM-CH, all 37 cells retained two separated nucleoid lobes (no DNA morphology change). For 10-min exposure to MM-CH, 18 of the 26 cells eventually showed the DNA coalescence behavior described above, even though the medium had been changed to EZRDM.

### Comparison of LL-37, cecropin A, and other synthetic copolymers

Finally, we tested the other agents in Table 1 for their ability to locally rigidify the chromosome and to induce coalescence of the two chromosomal DNA lobes. The results provide some insight into what features of an antimicrobial agent enable these effects. From the DNA locus tracking data taken at times greater than 25 min of treatment by each agent, we obtained the MSD plots shown in Fig. 2 A. The apparent diffusion coefficients  $D_{app}$  from linear fits to the first 10 data points are collected in Table 4. LL-37, MM-CH copolymer, and MM homopolymer rapidly rigidify local chromosomal motion almost as effectively as chemical fixation by formaldehyde. Cecropin A and the two shorter copolymers DM-DMCH and DM-DMCP reduced the DNA loci motion by a factor of 3–7 compared with normally growing cell. This is comparable to the effect of ATP depletion by the CCCP treatment. The diffusion coefficients of ribosomes under different treatments are also included in Table 4. The antimicrobial agents all slowed ribosome diffusion more than did ATP depletion.

Coalescence of the two nucleoid lobes on a 90-min timescale was induced only by MM-CH and by MM homopolymer. The natural AMPs LL-37 and cecropin A and the two shorter copolymers DM-DMCP and DM-DMCH did not cause coalescence on a 90-min timescale.

## DISCUSSION

### Short-term effects of cationic polymers and peptides

This study has compared the effects on *E. coli* of the six antimicrobial agents whose chemical compositions, contour lengths, and linear charge densities are given in Table 1. At  $2\times$  MIC, the long, highly charged copolymer MM-CH (11.5-nm mean contour length, mean charge +21, mean linear charge density  $+1.8$  e/nm) penetrates both the OM and CM remarkably quickly. Once MM-CH has permeabi-

lized both the CM and the OM to small molecules, there occurs a massive influx of highly positively charged copolymer into the cytoplasm. After gaining access to the cytoplasm, MM-CH causes several striking changes in the chromosomal DNA. On a timescale of  $\sim 5$ –10 min, the local jiggling motion of the DNA polymer is greatly attenuated, an effect we call rigidification of the nucleoid (6). On a similar timescale, the apparent volume of each of the two separate nucleoid lobes decreases by an estimated factor of  $\sim 1.7$ . On a much longer timescale of  $\sim 30$  min, in many of the cells one nucleoid lobe slowly migrates to coalesce with the other lobe, forming a dense, single-lobed nucleoid that strongly excludes ribosomal species. In many cases, this coalescence partially reverses on the timescale 60–90 min after initiation of copolymer flow. All of these same events were caused by the somewhat shorter (7.9 nm), but even more densely charged MM homopolymer ( $+22$ ,  $+2.8$  e/nm).

In contrast, the shorter DM-DMCP and DM-DMCH copolymers were less effective in rigidifying the DNA and did not cause large-scale coalescence of nucleoid lobes. DM-DMCP and DM-DMCH have similar charge densities as MM-CH, but different chemical compositions and also substantially shorter mean contour lengths (4.7 and 5.0 nm, respectively). The natural AMP LL-37 was as effective as MM-CH in locally rigidifying the DNA. The natural AMP cecropin A was less effective. Neither AMP caused large-scale nucleoid lobe coalescence.

As before (6), we suggest two underlying causes of the attenuation of the DNA jiggling motion. First, permeabilization of the CM and concomitant reduction in the transmembrane potential will slow or halt ATP production and presumably enable leakage of existing ATP to the cell surround.

This reduces the motor driven contribution to the jiggling motion of the DNA, as shown by the CCCP assay and observed earlier by others (27,28). This effect likely occurs for all six agents studied here. Second, we suggest that additional local rigidification of the DNA can be caused by “electrostatic pseudo-cross-linking” of nearby DNA strands within the dense nucleoid. Here, we envision transient, non-covalent binding of long polycationic species to release nearby  $K^+$  counterions and hinder the relative motion of adjacent DNA strands. The coarse-grained simulations of Chow and Skolnick (16) suggest typical gaps between nearby DNA strands of  $\sim 6$  nm. We suggest that longer molecules with high positive-charge density should accomplish this cross-linking more effectively. Accordingly, the MM-CH copolymer and MM homopolymer are quite long and densely charged. LL-37 is long but less densely charged. However, LL-37 has positive Lys and Arg residues at either end of the chain, enabling positive charges to span substantial gaps between DNA stands. Cecropin A concentrates its charges at its N-terminal half, rendering it less able to span large gaps with its positive charge.

The same pseudo-cross-linking effect may also explain the threefold decrease in the mean diffusion coefficient of HU (Fig. 2 B) induced by MM-CH on the 25-min timescale. The HU trajectories presumably involve an average over time spent diffusing “freely” (not bound to DNA) within the nucleoid and time spent bound to DNA. The coarse-grained simulation model of Chow and Skolnick (16) suggests that thermal motion of the DNA strands enables hopping of the transcription repressor protein LacI from one DNA cage within the nucleoid to an adjacent cage, a process they called “gated diffusion.” It seems plausible that the observed rigidification of the DNA would hinder gated diffusion. A similar reduction in HU diffusion is induced by MM homopolymer (Fig. 2 B) and by LL-37, the two agents that are most effective at DNA rigidification.

All six agents decrease the mean diffusion coefficient of ribosomal species 25 min after treatment by a factor the varies from 2 to 4 (Fig. 2 C), all larger effects than CCCP treatment. Each mean diffusion coefficient is an average over an unknown distribution of ribosomal species, including 30S subunits, 70S complete ribosomes, 70S polyosomes, and potentially agglomerations of such ribosomal species induced by the polycationic agent (29). Pseudo-cross-linking by polycationic agents may still occur between these negatively charged ribosome species to slow diffusion of ribosomes.

### Coacervation?

We have no clear understanding of the intriguing coalescence of the two nucleoid lobes induced at  $t \sim 30$  min, observed only for the longer, densely charged MM-CH copolymer and by the MM homopolymer, not for the other four agents. We tentatively suggest that this behavior is related to the well-known phenomenon of associative phase separation or coacervation (18,26,30). In certain equilibrium solution phase conditions, sufficiently long and densely charged polycations at sufficiently high concentration are able to condense DNA from its natural elongated, swollen structure into a compact structure via coacervation (26). There is in essence a phase separation between a polycation/polyanion rich phase and the remaining polymer-depleted portion of the solution.

A detailed study in vitro (26) found that 92-mer poly-L-lysine induces gradual compaction of DNA to a shrunken coil structure as the relative concentration of poly-L-lysine increases. The compaction was greatest when the ratio of total positive charges on the polycations to total negative charges on DNA reached one (17,26). The coacervation mechanism did not occur for short poly-L-lysine ( $n < 9$ ) (17,26). Small cations can compact DNA, but only at much higher concentrations (26).

The *E. coli* cytoplasm is dense with polyanionic species to which the polycationic MM-CH copolymer or MM homopolymer should bind strongly (31). As an upper limit,

we estimated that on average, each cell may absorb as many as  $\sim 10^9$  positive charges carried by the MM-CH copolymer. For a typical total cell volume of  $\sim 1.9 \mu\text{m}^3$ , this corresponds to an average concentration of  $\sim 0.9$  M of polymeric positive charge, a very large number. Under our growth conditions we estimate that cytoplasmic polyanionic species (chromosome, ribosome, transfer RNA (tRNA), mRNA) provide  $\sim 2 \times 10^8$  negative charges ( $\sim 200$  mM); these are compensated primarily by  $\text{K}^+$  (Supporting materials and methods). It is plausible that sufficient MM-CH is absorbed within the cytoplasm to cause coacervation with the chromosomal DNA.

Before the addition of MM-CH, the chromosomal DNA is already highly compacted due to pairwise binding by a variety of nucleoid-associated proteins (17,19,32–34); segregative phase separation due to DNA-ribosome repulsion (19,35,36); configurational entropy of the confined DNA polymer to avoid the cell boundaries (37); neutralization of DNA charges by multivalent ions and some DNA-binding proteins; macromolecular crowding (17,30,38,39); and DNA supercoiling (17,33,40,41). Nevertheless, as MM-CH gains access to the cytoplasm we observe significant radial shrinkage of the two nucleoid lobes, with the mean radius decreasing from 0.29 to 0.22  $\mu\text{m}$  (for cells in 4–4.3  $\mu\text{m}$  length range, Fig. S5). The nucleoid volume decreases by a factor of  $\sim 1.7$ . This is consistent with the suggestion that MM-CH causes coacervation of the chromosomal DNA before the longer-term coalescence of the two nucleoid lobes. In contrast, in the earlier study LL-37 did not contract the nucleoid volume. LL-37 is likely insufficiently positive and too short to induce this effect.

The coacervation hypothesis may also provide a partial explanation for the observed slow migration of one nucleoid lobe to coalesce with the other lobe. In solution phase, coacervate droplets have been observed to coalesce with each other over time, perhaps to minimize surface tension with the surrounding phase (42,43). Similar behavior of liquid droplets has been observed in eukaryotic cells (44–46). We lack a good rationale for the slow reversal from the one-lobed, coalesced condition back toward the original two-lobed condition. On the 90-min timescale of a video (Video S1, Video S2), this occurs in roughly half of the that showed coalescence. Concentrations of the myriad species within the cytoplasm continue to change as the concentration of absorbed polymer increases. The coacervation process occurs at a narrow concentration ratio range for polycations and polyanions (18,43,47,48).

### CONCLUSIONS

To date, all of our time-resolved, single-cell mechanistic studies have used linear, polycationic antibacterial agents, including both AMPs of defined sequence and sequence-random polymers (6,9–11,49). Does permeabilization of the bacterial membranes by these agents cause the halting

of growth? Our experience supports the conclusion that there is a threshold concentration above which permeabilization of the OM occurs; below that concentration cells continue to grow, albeit sometimes more slowly. Permeabilization of the CM then occurs rapidly and eventually growth halts in a seemingly irreversible fashion. CM permeabilization destroys the transmembrane potential and rapidly causes loss of the cell surround of small molecules such as ATP and perhaps of globular proteins and tRNA. These same cationic agents may also interfere with a wide variety of cellular processes including cell envelope biosynthesis, DNA replication and transcription, and protein synthesis (2,4,5). A surprising effect that is beginning to seem quite general is the massive uptake of polycationic agents once the OM and CM have been breached (6–8). A bacterial cytoplasm exposed to the surround appears to be a sponge that soaks up polycations to very high internal concentrations ( $10^8$ – $10^9$  positive charges). Again, we suggest that the key driving force is strong, noncovalent, multivalent electrostatic binding between polycations and polyanions (DNA, ribosomes, mRNA, tRNA, and even globular proteins) (19,31). Nature has designed a bacterial cytoplasm that is remarkably susceptible to damage by polycationic agents. At least for linear, polycationic agents, our view is that membrane permeabilization appears to be a necessary first step leading to a cascade of downstream events, many occurring on a timescale of a few minutes or less. With so many effects likely occurring on a similar timescale, it is difficult to attribute the halting of growth (and apparent killing of cells) to any single event, but membrane permeabilization is the necessary triggering event.

This work on cationic polymers highlights several new effects: rigidification of the DNA and attenuation of ribosome and protein diffusion on a short timescale of several minutes and coalescence of the two nucleoid lobes at longer times of 30 min or more. The recovery experiments show that the cells absorb sufficient MM-CH copolymer during the first 5 min of exposure to prevent subsequent growth for at least 90 min after the flow had switched to fresh EZRDM without copolymer. These same cells do not subsequently show DNA coalescence or gross content leakage (no white band on phase contrast image). Evidently sufficient MM-CH enters the cells in 5 min to induce enough damage to halt growth. In contrast, after a 10 min exposure to MM-CH followed by 90 min in fresh EZRDM, cells eventually show both nucleoid coalescence and complete membrane disruption. The additional polymer absorbed over the interval from 5 to 10 min seems essential to drive the long-term nucleoid coalescence. Such coalescence is evidently not necessary to halt growth—only a fraction of the cells exhibited this behavior. In addition, all six of the tested agents halt the growth of *E. coli*, but some agents cause the long-term coalescence of the two nucleoid lobes and others do not. It also seems unlikely that DNA rigidification is necessary to halt

growth. The agents exhibit widely varying degrees of DNA rigidification and diffusion attenuation.

Finally, we find it remarkable that the sequence-random, cationic polymers studied here are so readily able to traverse the OM and CM of *E. coli*. This result seems incompatible with models of membrane disruption that posit formation of structured pores, either toroidal or barrel-stave.

## SUPPORTING MATERIAL

Supporting material can be found online at <https://doi.org/10.1016/j.bpj.2021.10.037>.

## AUTHOR CONTRIBUTIONS

Y.Z. and M.M. carried out the microscopy studies. L.L., L.A.R., and S.H.G. designed, synthesized, and characterized the polymer samples. Y.Z. and J.C.W. planned the microscopy studies and wrote the article, with help from L.L. and S.H.G.

## ACKNOWLEDGMENTS

J.C.W. thanks the Wisconsin Alumni Research Foundation for a faculty fellowship. We thank Prof. Arun Yethiraj, Dr. Tyler Lytle, and Dr. Sonisilpa Mohapatra for helpful discussions.

This work was supported by the National Institutes of Health (grants R01-GM094510 to J.C.W. and R33-AI121684 to S.H.G.) and by the National Science Foundation (grant MCB-1512946 to J.C.W.). The content is solely the responsibility of the authors and does not necessarily represent the official views of the National Institutes of Health.

## REFERENCES

1. Savini, F., S. Bobone, ..., L. Stella. 2018. From liposomes to cells: filling the gap between physicochemical and microbiological studies of the activity and selectivity of host-defense peptides. *Peptide Science*. 110:e24041.
2. Brogden, K. A. 2005. Antimicrobial peptides: pore formers or metabolic inhibitors in bacteria? *Nat. Rev. Microbiol.* 3:238–250.
3. Zasloff, M. 2002. Antimicrobial peptides of multicellular organisms. *Nature*. 415:389–395.
4. Scocchi, M., M. Mardirossian, ..., M. Benincasa. 2016. Non-membrane permeabilizing modes of action of antimicrobial peptides on bacteria. *Curr. Top. Med. Chem.* 16:76–88.
5. Zhu, Y., J. C. Weisshaar, and M. Mustafi. 2020. Long-term effects of the proline-rich antimicrobial peptide Oncocin112 on the *Escherichia coli* translation machinery. *J. Biol. Chem.* 295:13314–13325.
6. Zhu, Y., S. Mohapatra, and J. C. Weisshaar. 2019. Rigidification of the *Escherichia coli* cytoplasm by the human antimicrobial peptide LL-37 revealed by superresolution fluorescence microscopy. *Proc. Natl. Acad. Sci. USA*. 116:1017–1026.
7. Roversi, D., V. Luca, ..., L. Stella. 2014. How many antimicrobial peptide molecules kill a bacterium? The case of PMAP-23. *ACS Chem. Biol.* 9:2003–2007.
8. Starr, C. G., J. He, and W. C. Wimley. 2016. Host cell interactions are a significant barrier to the clinical utility of peptide antibiotics. *ACS Chem. Biol.* 11:3391–3399.
9. Choi, H., N. Rangarajan, and J. C. Weisshaar. 2016. Lights, camera, action! Antimicrobial peptide mechanisms imaged in space and time. *Trends Microbiol.* 24:111–122.

10. Yang, Z., H. Choi, and J. C. Weisshaar. 2018. Melittin-induced permeabilization, re-sealing, and re-permeabilization of *E. coli* membranes. *Biophys. J.* 114:368–379.
11. Choi, H., S. Chakraborty, ..., J. C. Weisshaar. 2016. Single-cell, time-resolved antimicrobial effects of a highly cationic, random nylon-3 copolymer on live *Escherichia coli*. *ACS Chem. Biol.* 11:113–120.
12. Mowery, B. P., S. E. Lee, ..., S. H. Gellman. 2007. Mimicry of antimicrobial host-defense peptides by random copolymers. *J. Am. Chem. Soc.* 129:15474–15476.
13. Mowery, B. P., A. H. Lindner, ..., S. H. Gellman. 2009. Structure-activity relationships among random nylon-3 copolymers that mimic antibacterial host-defense peptides. *J. Am. Chem. Soc.* 131:9735–9745.
14. Liu, R., X. Chen, ..., S. H. Gellman. 2014. Tuning the biological activity profile of antibacterial polymers via subunit substitution pattern. *J. Am. Chem. Soc.* 136:4410–4418.
15. Rank, L. A., A. Agrawal, ..., S. H. Gellman. 2021. Diverse impacts on prokaryotic and eukaryotic membrane activities from hydrophobic subunit variation among nylon-3 copolymers. *ACS Chem. Biol.* 16:176–184.
16. Chow, E., and J. Skolnick. 2017. DNA internal motion likely accelerates protein target search in a packed nucleoid. *Biophys. J.* 112:2261–2270.
17. Joyeux, M. 2015. Compaction of bacterial genomic DNA: clarifying the concepts. *J. Phys. Condens. Matter* 27:383001.
18. van der Gucht, J., E. Spruijt, ..., M. A. Cohen Stuart. 2011. Polyelectrolyte complexes: bulk phases and colloidal systems. *J. Colloid Interface Sci.* 361:407–422.
19. Joyeux, M. 2016. In vivo compaction dynamics of bacterial DNA: a fingerprint of DNA/RNA demixing? *Curr. Opin. Colloid Interface Sci.* 26:17–27.
20. Estevez-Torres, A., and D. Baigl. 2011. DNA compaction: fundamentals and applications. *Soft Matter* 7:6746–6756.
21. Sochacki, K. A., I. A. Shkel, ..., J. C. Weisshaar. 2011. Protein diffusion in the periplasm of *E. coli* under osmotic stress. *Biophys. J.* 100:22–31.
22. Espeli, O., R. Mercier, and F. Boccard. 2008. DNA dynamics vary according to macrodomain topography in the *E. coli* chromosome. *Mol. Microbiol.* 68:1418–1427.
23. Cavari, B. Z., and Y. Avi-Dor. 1967. Effect of carbonyl cyanide *m*-chlorophenylhydrazine on respiration and respiration-dependent phosphorylation in *Escherichia coli*. *Biochem. J.* 103:601–608.
24. Zhu, Y., M. Mustafi, and J. C. Weisshaar. 2020. Biophysical properties of *Escherichia coli* cytoplasm in stationary phase by superresolution fluorescence microscopy. *MBio*. 11:e00143-20.
25. Bakshi, S., H. Choi, ..., J. C. Weisshaar. 2014. Nonperturbative imaging of nucleoid morphology in live bacterial cells during an antimicrobial peptide attack. *Appl. Environ. Microbiol.* 80:4977–4986.
26. Akitaya, T., A. Seno, ..., K. Yoshikawa. 2007. Weak interaction induces an ON/OFF switch, whereas strong interaction causes gradual change: folding transition of a long duplex DNA chain by poly-L-lysine. *Biomacromolecules*. 8:273–278.
27. Weber, S. C., A. J. Spakowitz, and J. A. Theriot. 2012. Nonthermal ATP-dependent fluctuations contribute to the in vivo motion of chromosomal loci. *Proc. Natl. Acad. Sci. USA*. 109:7338–7343.
28. Parry, B. R., I. V. Surovtsev, ..., C. Jacobs-Wagner. 2014. The bacterial cytoplasm has glass-like properties and is fluidized by metabolic activity. *Cell*. 156:183–194.
29. Chongsiriwatana, N. P., J. S. Lin, ..., A. E. Barron. 2017. Intracellular biomass flocculation as a key mechanism of rapid bacterial killing by cationic, amphipathic antimicrobial peptides and peptoids. *Sci. Rep.* 7:16718.
30. Lerman, L. S. 1971. A transition to a compact form of DNA in polymer solutions. *Proc. Natl. Acad. Sci. USA*. 68:1886–1890.
31. Schavemaker, P., W. Smigiel, and B. Poolman. 2017. Ribosome surface properties may impose limits on the nature of the cytoplasmic proteome. *Elife*. 6:e30084.
32. Song, D., and J. J. Loparo. 2015. Building bridges within the bacterial chromosome. *Trends Genet.* 31:164–173.
33. Wang, X., P. Montero Llopis, and D. Z. Rudner. 2013. Organization and segregation of bacterial chromosomes. *Nat. Rev. Genet.* 14:191–203.
34. Wang, W., G. W. Li, ..., X. Zhuang. 2011. Chromosome organization by a nucleoid-associated protein in live bacteria. *Science*. 333:1445–1449.
35. Krotova, M. K., V. V. Vasilevskaya, ..., A. R. Khokhlov. 2010. DNA compaction in a crowded environment with negatively charged proteins. *Phys. Rev. Lett.* 105:128302.
36. Yoshikawa, K., S. Hirota, ..., Y. Yoshikawa. 2010. Compaction of DNA induced by like-charge protein: opposite salt-effect against the polymer-salt-induced condensation with neutral polymer. *J. Phys. Chem. Lett.* 1:1763–1766.
37. Mondal, J., B. P. Bratton, ..., J. C. Weisshaar. 2011. Entropy-based mechanism of ribosome-nucleoid segregation in *E. coli* cells. *Biophys. J.* 100:2605–2613.
38. Asakura, S., and F. Oosawa. 1954. On interaction between 2 bodies immersed in a solution of macromolecules. *J. Chem. Phys.* 22:1255–1256.
39. Teif, V. B., and K. Bohinc. 2011. Condensed DNA: condensing the concepts. *Prog. Biophys. Mol. Biol.* 105:208–222.
40. Benza, V. G., B. Bassetti, ..., M. C. Lagomarsino. 2012. Physical descriptions of the bacterial nucleoid at large scales, and their biological implications. *Rep. Prog. Phys.* 75:076602.
41. Postow, L., C. D. Hardy, ..., N. R. Cozzarelli. 2004. Topological domain structure of the *Escherichia coli* chromosome. *Genes Dev.* 18:1766–1779.
42. Priftis, D., R. Farina, and M. Tirrell. 2012. Interfacial energy of polypeptide complex coacervates measured via capillary adhesion. *Langmuir*. 28:8721–8729.
43. Sing, C. E. 2017. Development of the modern theory of polymeric complex coacervation. *Adv. Colloid Interface Sci.* 239:2–16.
44. Deshpande, S., F. Brandenburg, ..., C. Dekker. 2019. Spatiotemporal control of coacervate formation within liposomes. *Nat. Commun.* 10:1800.
45. Astoricchio, E., C. Alfano, ..., A. Pastore. 2020. The wide world of coacervates: from the sea to neurodegeneration. *Trends Biochem. Sci.* 45:706–717.
46. Shin, Y., and C. Brangwynne. 2017. Liquid phase condensation in cell physiology and disease. *Science*. 357:eaaf4382.
47. Lytle, T. K., and C. E. Sing. 2017. Transfer matrix theory of polymer complex coacervation. *Soft Matter*. 13:7001–7012.
48. Singh, A. N., and A. Yethiraj. 2020. Driving force for the complexation of charged polypeptides. *J. Phys. Chem. B*. 124:1285–1292.
49. Sochacki, K. A., K. J. Barns, ..., J. C. Weisshaar. 2011. Real-time attack on single *Escherichia coli* cells by the human antimicrobial peptide LL-37. *Proc. Natl. Acad. Sci. USA*. 108:E77–E81.

**Biophysical Journal, Volume 120**

**Supplemental information**

**Local rigidification and possible coacervation of the *Escherichia coli*  
DNA by cationic nylon-3 polymers**

**Yanyu Zhu, Lei Liu, Mainak Mustafi, Leslie A. Rank, Samuel H. Gellman, and James C. Weisshaar**

**Table S1.** Characterization of nylon-3 polymers.

<b>Polymer</b>	<b><math>\bar{D}_{GPC}^a</math></b>	<b><math>M_{nGPC}^b</math></b>	<b><math>D_{pNMR}^c</math></b>	<b><math>M_{NMR}^d</math></b>
MM-CH	1.070	7841	32	3954
MM homopolymer	1.167	2038	22	2693
DM-DMCP	1.08	6538	13	1879
DM-DMCH	1.08	3235	14	2041

<sup>a</sup> Polymer length dispersity =  $M_w/M_n$ .

<sup>b</sup> The number-averaged molecular weight of side-chain protected polymers determined from GPC.

<sup>c</sup> The degree of polymerization, or average polymer chain length, as calculated by NMR integrations based on end group analysis, i.e., the assumption that each chain contains only one *tert*-butyl benzoyl group.

<sup>d</sup> Average molecular weight of side-chain deprotected polymers calculated based on NMR. The polymers are in the form of trifluoroacetate salts. The polymers are used in the form of aqueous solution, so the molecular weight of trifluoroacetate counter anions are not included.

**Table S2.** Bacterial strains

<b>Strain</b>	<b>Species imaged</b>	<b>Strain details</b>	<b>Background strain</b>	<b>Expression method</b>
JCW154	<i>Right2-parS</i> by ParB-GFP	Ref. (1)	MG1655	Plasmid
JCW10	Periplasmic GFP	Ref. (2)	MG1655	Plasmid
MDG196	Ribosome S2-mEos2	Ref. (3)	VH1000	Chromosome
MSG192	Ribosome S2-YFP	Ref. (4,5)	VH1000	Chromosome
MG1655	WT	—	MG1655	—
VH1000	WT	—	VH1000	—
SM7	HU-PAmCherry	Ref. (5)	VH1000	Plasmid
Dendra2	Ribosome S2-Dendra2	Ref. (6)	MG1655	Chromosome

## Explanation of Videos

### Video S1

Corresponding to data in Fig. 1. Effects of copolymer MM-CH on a representative *E. coli* cell that exports GFP to the periplasm. Phase contrast image (left), fluorescence snapshots of GFP (middle) and Sytox Orange (right) are shown. Flow of 2× MIC of MM-CH in EZRDM with 5 nM of the DNA stain Sytox Orange begins at  $t = 0$ . Images were acquired at 12 s per frame for 90 min.

### Video S2

Corresponding to data in Fig. 3E. Phase contrast image (left), Sytox Orange fluorescence (middle) and ribosome S2-YFP fluorescence (right) snapshots of single *E. coli* cell at different times during the attack of copolymer MM-CH are shown. Cells with ribosomal S2 subunit labeled with YFP were stained with 500 nM Sytox Orange for 10 min before imaging. 2× MIC MM-CH flowed beginning at  $t = 0$ . Images were acquired at 1 min per frame for 90 min.

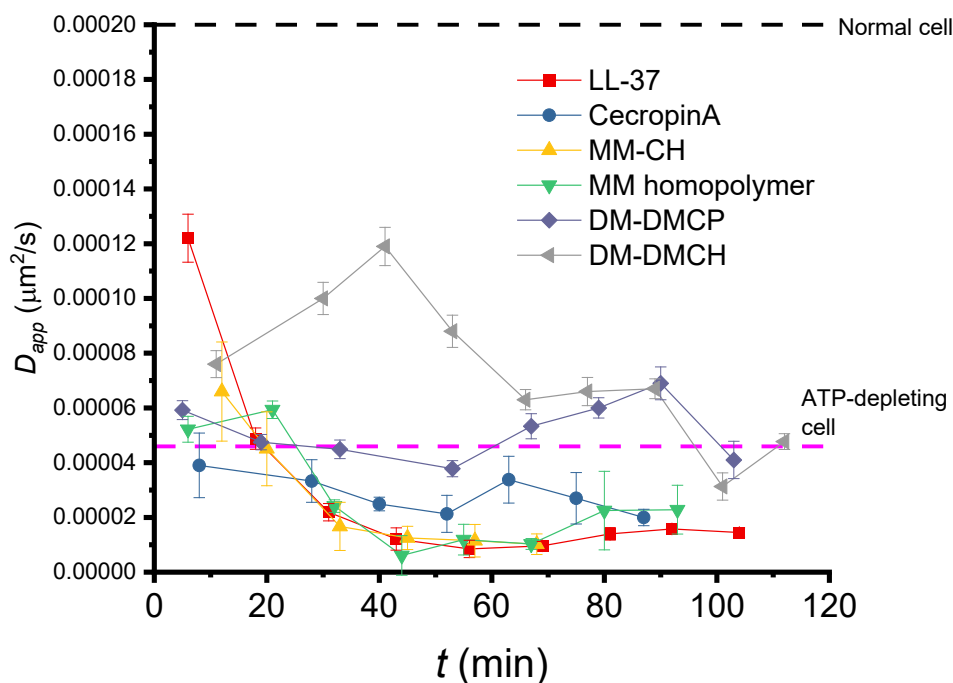


**Figure S1.** Apparent diffusion coefficient of DNA loci as a function of time after the onset of treatment with AMP or polymer at  $t = 0$ . Each time point represents the average over a 10-min window with images taken at 1s/frame. The time plotted for each point is the center of the 10-min window. The apparent diffusion coefficient  $D$  is obtained from a linear fit to the first 10 points in the MSD plot. Reference value for normal cells and ATP depleted cells are shown as the black dashed line and purple dashed line.

## Ribosome Diffusion

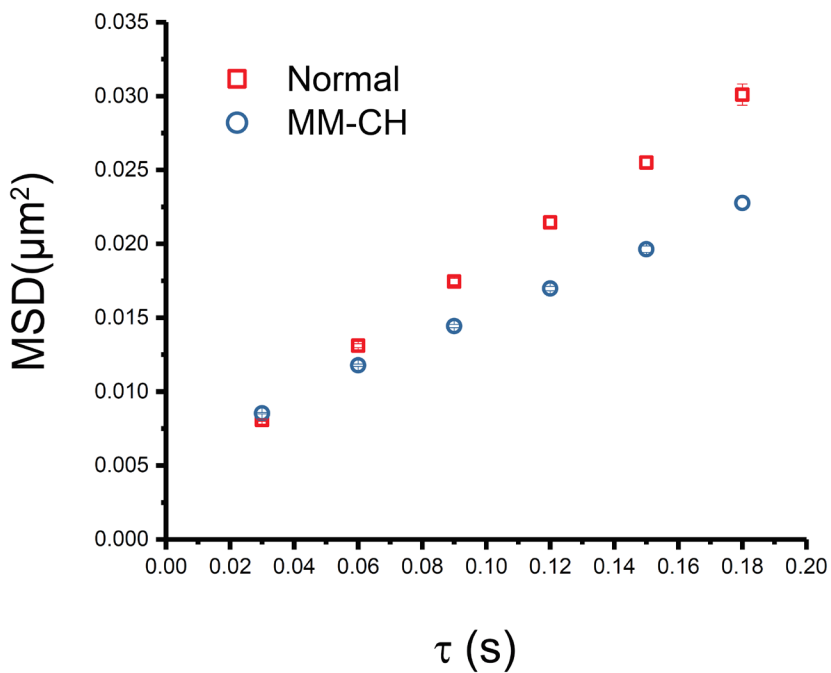


**Figure S2.** Ribosomal species MSD vs lag time from S2-Dendra2 trajectories taken at 30 ms/frame in two different conditions as shown. The apparent diffusion coefficient  $D_{app}$  is obtained by linear fitting of the first three data points. The numerical results are:  $(0.039 \pm 0.002)$   $\mu\text{m}^2/\text{s}$  for normal growth;  $(0.025 \pm 0.001)$   $\mu\text{m}^2/\text{s}$  for cells 25 min after onset of MM-CH treatment.



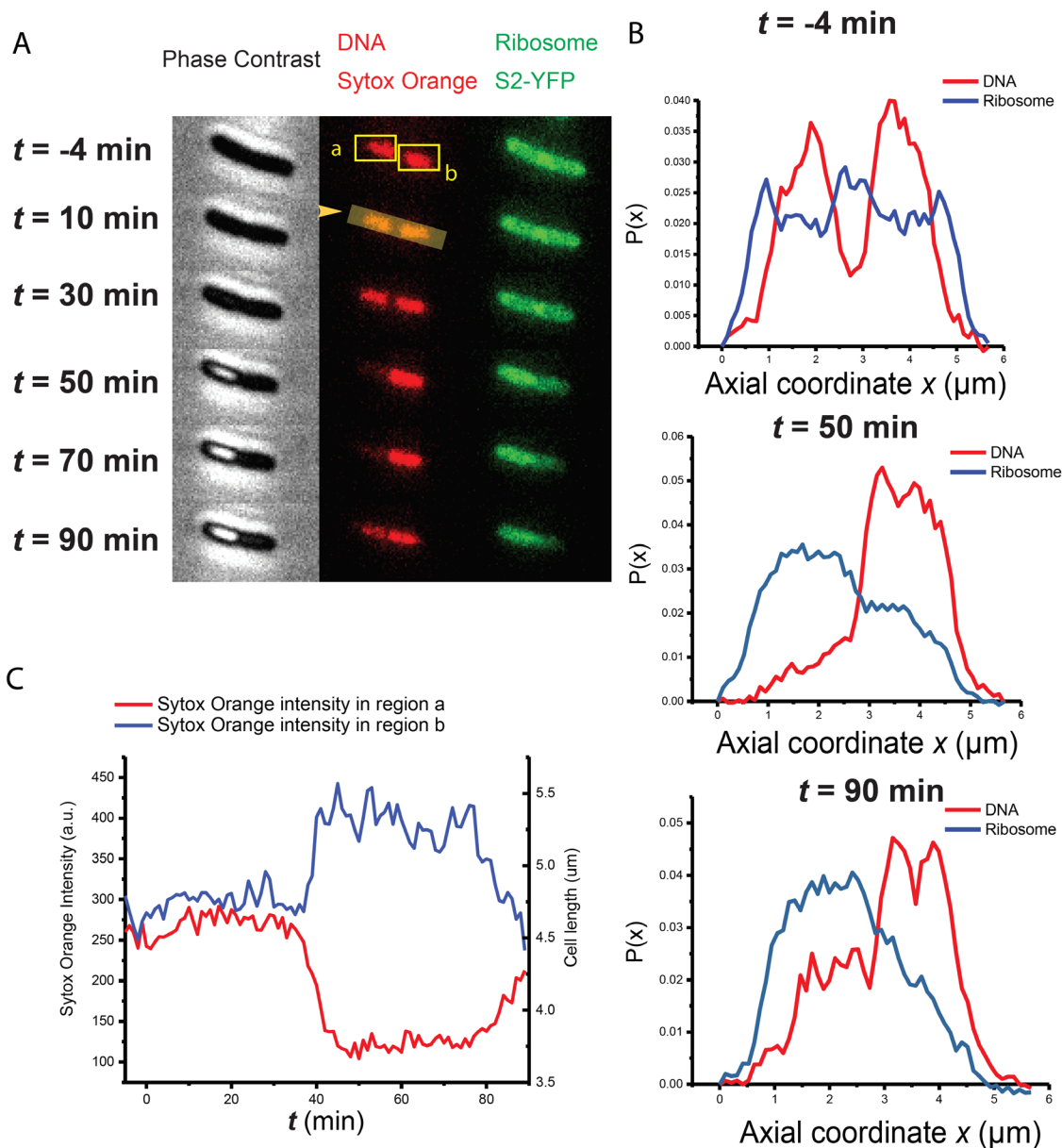


**Figure S3.** Ribosome-DNA segregation throughout large-scale nucleoid morphology changes. Cells with ribosome S2 subunit labeled with YFP were stained with 500 nM Sytox Orange for 10 min before imaging.  $2\times$  MIC MM-CH flowed beginning at  $t = 0$ . Images were acquired at 1 min per frame. (A) Phase contrast, Sytox Orange fluorescence and ribosome S2-YFP snapshots of single *E. coli* cell at different times. (B) For the same cell shown in (A), projected axial Sytox Orange and YFP projected axial intensity profiles (direction of arrowhead in panel (A)). (C) Sytox Orange intensity vs time for the same cell shown in panel (A). Sytox Orange intensity in the left nucleoid lobe (red curve, region a in panel (A)), and in the right nucleoid lobe (blue curve, region b in panel (A)) are shown separately.

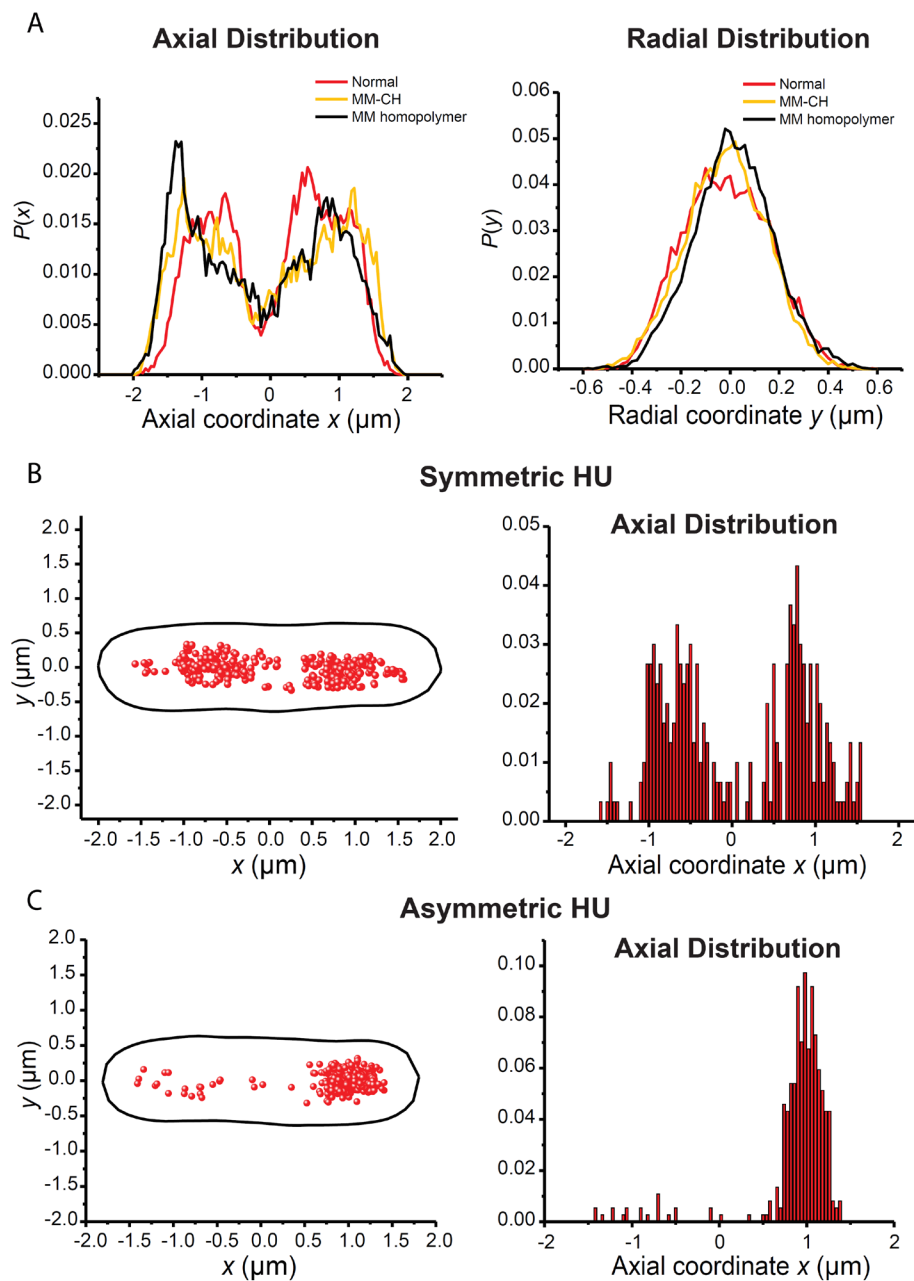


**Figure S4.** HU-PAMCherry super-resolution spatial distribution imaged in normal cells and after treatment with polymer. (A) Cell-averaged HU spatial distribution in cells with length of 4.0–4.3  $\mu\text{m}$ . Projected axial (*left*) and radial (*right*) distribution of HU in normal cells and 25 min after the onset of MM-CH copolymer and MM homopolymer treatment. Radial distribution includes only molecules in the nucleoid region ( $0.4 \mu\text{m} < |x| < 1.2 \mu\text{m}$ ). (B,C) Two examples of single-cell DNA (HU-PAMCherry) spatial distributions exhibiting after MM-CH treatment. The cell in panel B shows two symmetric axial lobes, whereas the cell in panel C shows asymmetric lobes. *Left*: scatter plot of HU locations. Black line is cell mesh generated from phase contrast image using Oufiti program. *Right*: axial distribution of HU locations.

## Singel Cell HU Radial Distribution

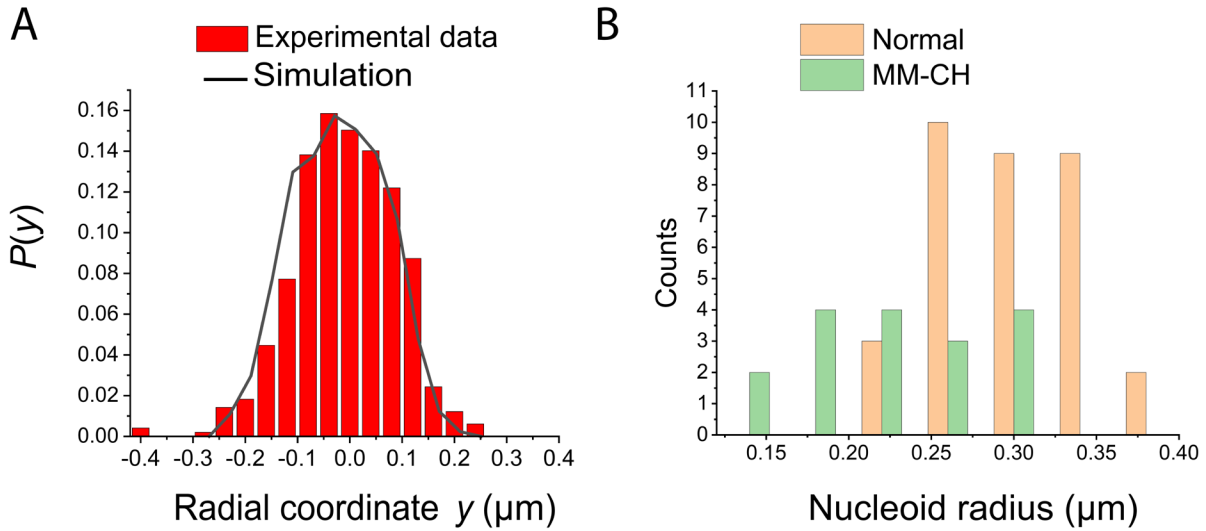


**Figure S5.** Quantitative determination of nucleoid radius in normal cells and after treatment with MM-CH. (A) Single cell HU radial distributions (red) of an example cell with cell length 4.1  $\mu\text{m}$ . Black lines: simulated radial projections of particles uniformly distributed within a spherocylinder of radius  $r = 0.16 \mu\text{m}$ . (B) Distribution of single-cell nucleoid radii for cells in normal growth condition and 25 min after 2X MIC MM-CH with two nucleoid lobes. Only cells in the length range of 4.0-4.3  $\mu\text{m}$  are included. For each cell, the radius was determined by fitting the HU nucleoid radial distributions with calculated projections from a uniform distribution within a spherocylinder. Radius was varied to find the best fit.

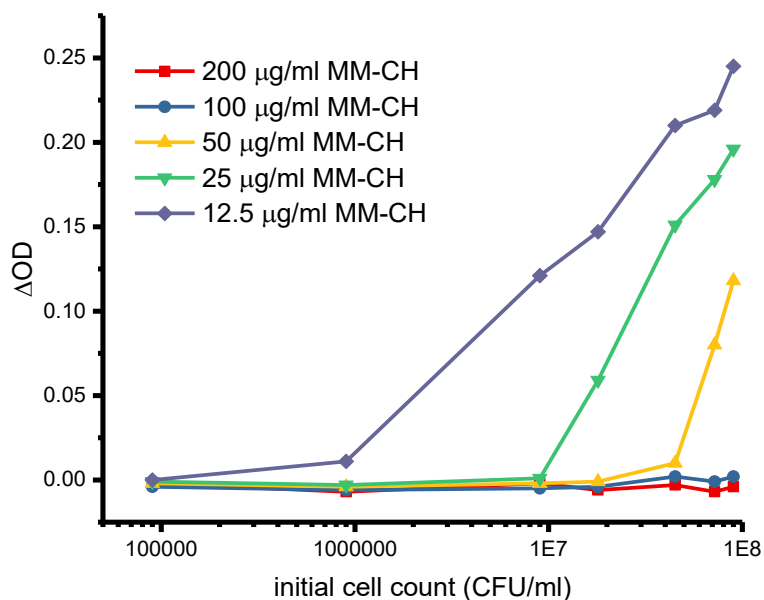


**Figure S6.** Determination of the MM-CH initial concentration required to kill a given concentration of bacterial cells. For each MM-CH concentration and for each initial cell count, we measured the optical density (OD) at 595 nm before and after 24-hour incubation of the cells with MM-CH. The change in OD is defined as  $\Delta OD = OD_{t=24h} - OD_{t=0}$ . For a given MM-CH concentration, as the CFU/ml increases,  $\Delta OD$  becomes significantly greater than zero when the initial number of cells becomes too large to be completely killed by the MM-CH concentration provided.

## GPC and NMR characterization of nylon-3 polymers

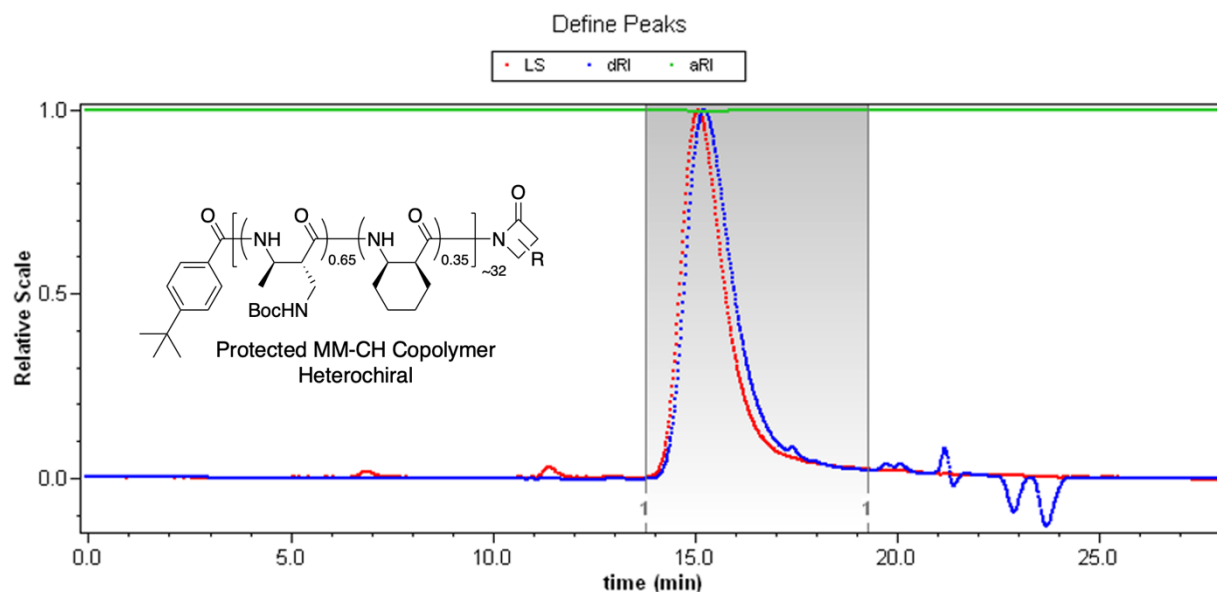


**Figure S7.** GPC chromatogram of MM-CH (Boc protected amine) copolymer, with the mobile phase of THF at 40°C. Red line represents detection via light scattering (LS), and blue line represents detection via differential refractive index (dRI). The LS peak eluting from 6 to 8 minutes is attributed to a large molecule weight polymer from the column stationary phase.

Polymer	$\bar{D}_{\text{GPC}}$	Mn
MM-CH	1.07	7841



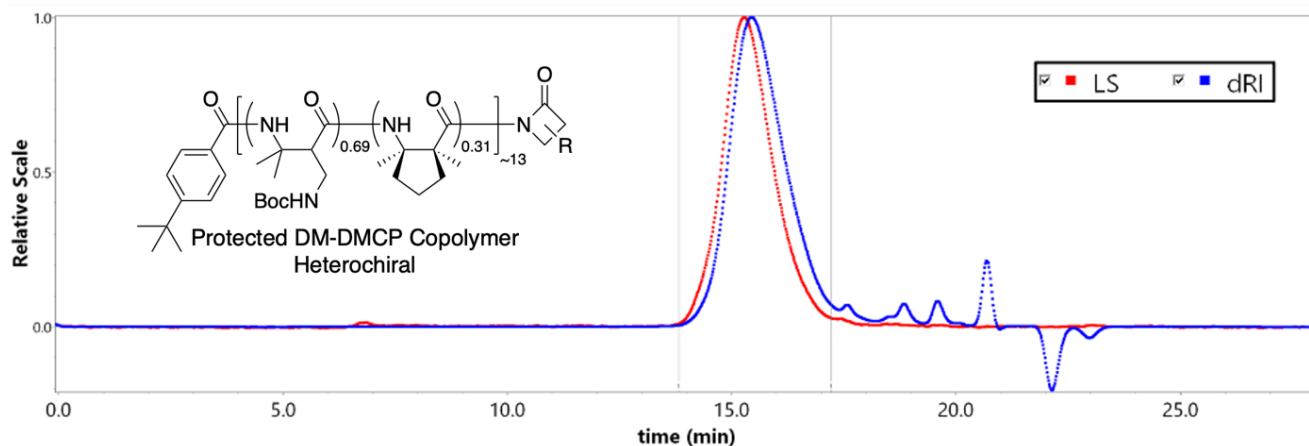


**Figure S9.** GPC chromatogram of DM-DMCP (Boc protected amine) copolymer, with the mobile phase of THF at 40°C. Red line represents detection via light scattering (LS), and blue line represents detection via differential refractive index (dRI). The LS peak eluting from 6 to 8 minutes is attributed to a large molecule weight polymer from the column stationary phase.

Polymer	$D_{\text{GPC}}$	Mn
DM-DMCP	1.08	6538

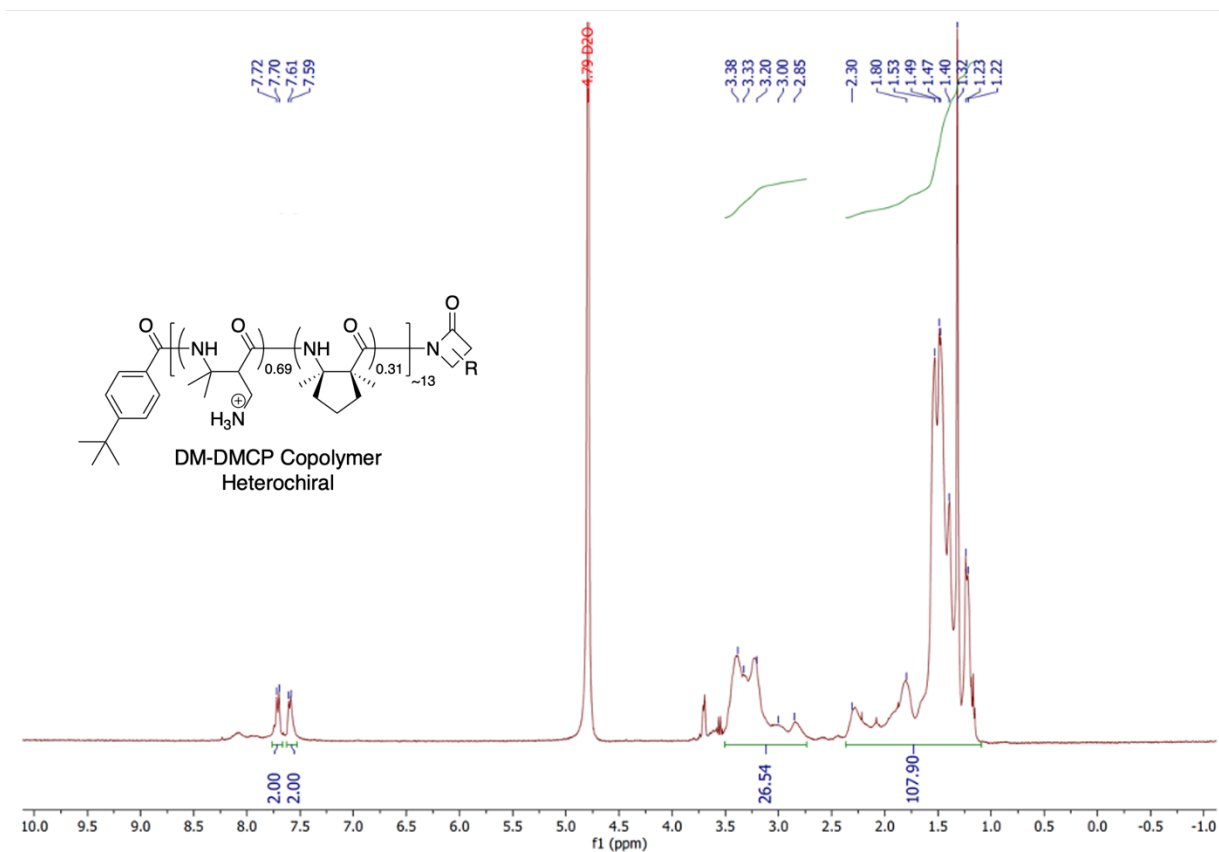


**Figure S10.**  $^1H$  NMR spectrum (500 MHz,  $D_2O$ ) of DM-DMCP deprotected copolymers.

Calculations for  $D_{p_{NMR}}$  and subunit ratio of DM-DMCP copolymer:

$$26.54 = 3 \text{ DM protons}$$

$$107.90 = 6 \text{ DM protons} + 12 \text{ DMCP protons} + 9 \text{ Initiator protons}$$

$$DM \approx 9 \text{ and DMCP} \approx 4$$

$$D_{p_{NMR}} = DM + DMCP = 13$$



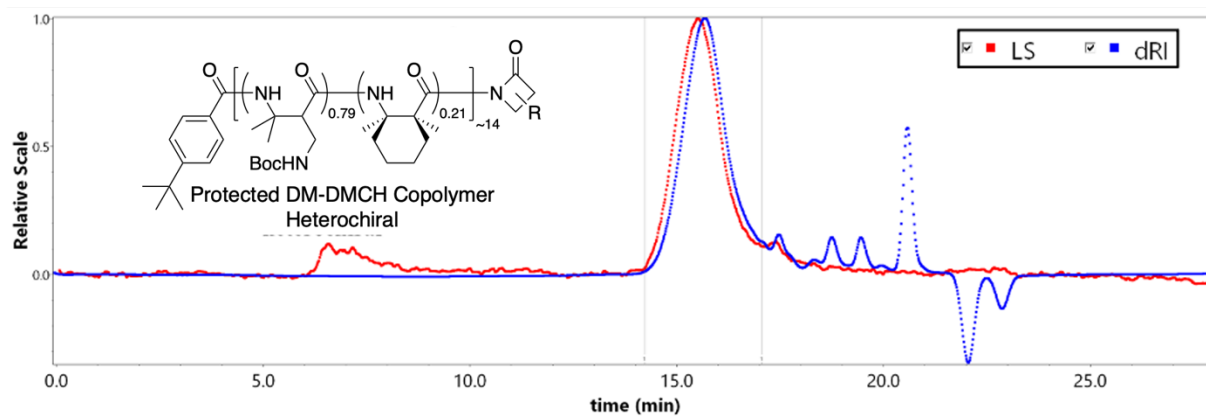


**Figure S11.** GPC chromatogram of DM-DMCH (Boc protected amine) copolymer, mobile phase THF, 40°C. Red line represents detection via light scattering (LS), and blue line represents detection via differential refractive index (dRI). The LS peak eluting from 6 to 8 minutes is attributed to a large molecule weight polymer shed from the column stationary phase.

Polymer	$\bar{D}_{\text{GPC}}$	Mn
DM-DMCH	1.08	3235

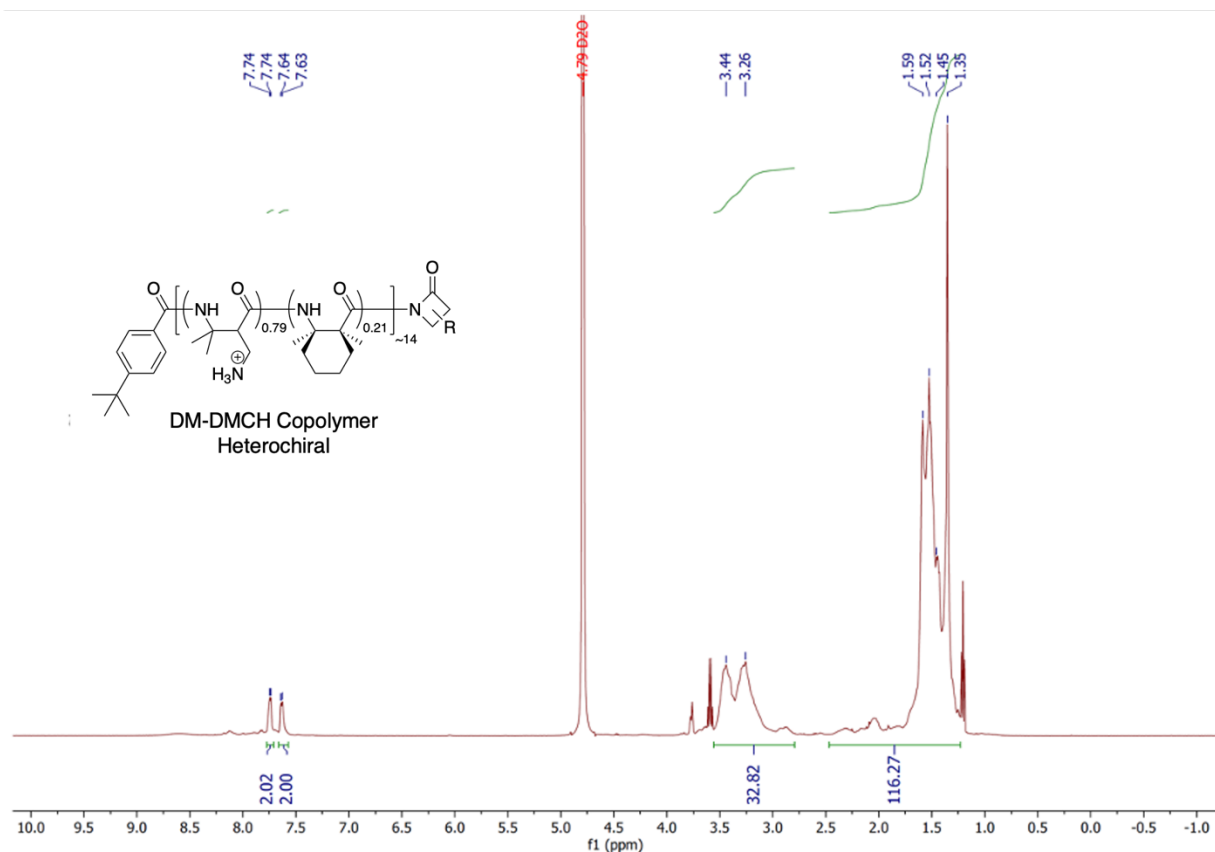


**Figure S12.** <sup>1</sup>H NMR spectrum (500 MHz, D<sub>2</sub>O) of DM-DMCH deprotected copolymers.

Calculations for  $D_{p,NMR}$  and subunit ratio of DM-DMCH copolymer:

32.82 = 3 DM protons

116.27 = 6 DM protons + 14 DMCH protons + 9 Initiator protons

DM ≈ 11 and DMCH ≈ 3

$DP_{NMR} = DM + DMCH = 14$

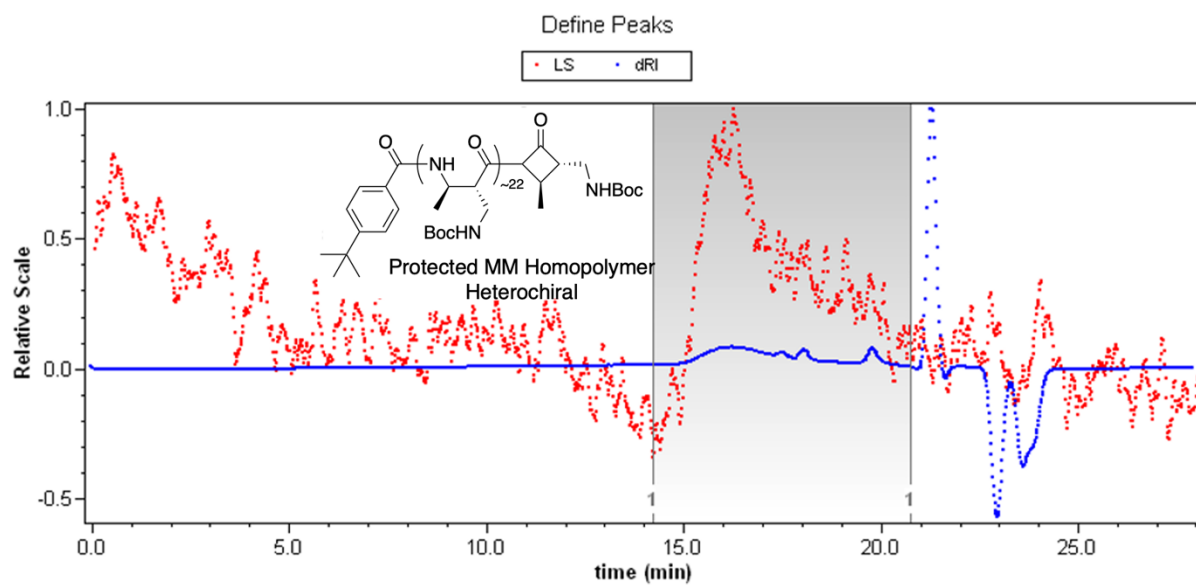


**Figure S13.** GPC chromatogram of MM (Boc protected amine) homopolymer, mobile phase THF, 40°C. Red line represents detection via light scattering (LS), and blue line represents detection via differential refractive index (dRI).

Polymer	$\bar{D}_{\text{GPC}}$	Mn
MM Homopolymer	1.17	2038

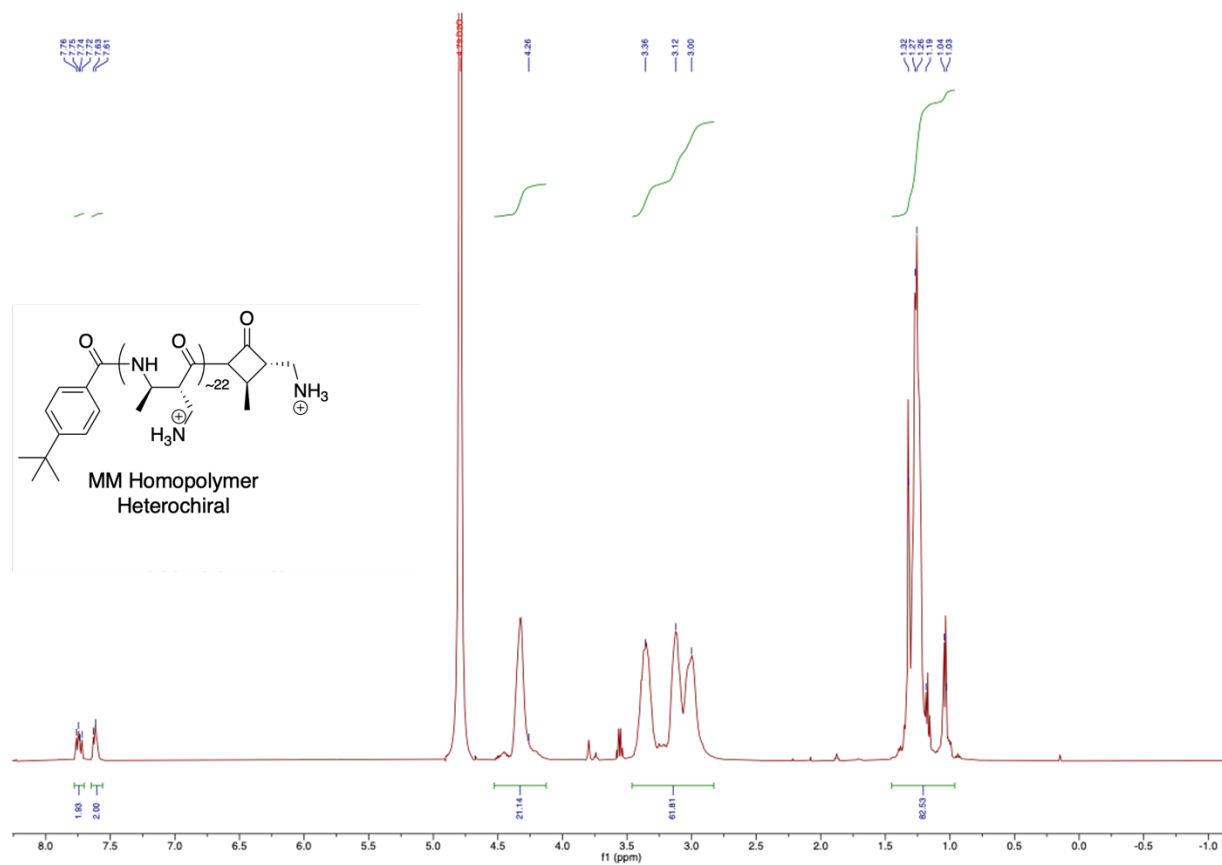


**Figure S14.**  $^1\text{H}$  NMR spectrum (500 MHz,  $\text{D}_2\text{O}$ ) of deprotected MM homopolymer.

Calculations for  $\text{Dp}_{\text{NMR}}$  and subunit ratio of MM homopolymer:

21.14 = 1 MM proton

61.81 = 3 MM protons

82.53 = 3 MM protons + 9 Initiator protons

MM  $\approx$  22

$\text{DP}_{\text{NMR}} = 22$

## Synthesis of Nylon-3 polymers

The  $\beta$ -lactam solution in tetrahydrofuran (THF) was added a solution of the co-initiator precursor, *p*-tert-butylbenzoyl chloride in THF (7). The amount of the co-initiator depended on the intended degree of polymerization. For instance, for an average chain length of 20, 0.05 equivalents of the co-initiator precursor relative to the total quantity of  $\beta$ -lactam monomers was used in the polymerization reaction. Then a solution of lithium bis(trimethylsilyl)amide in THF (2.5 equivalents of this base relative to the amount of *p*-tert-butylbenzoyl chloride) was added, and the mixture was stirred overnight at room temperature. A few drops of methanol were added to the reaction to quench the polymerization reactions. Then polymers were isolated by precipitation with pentanes. Copolymers at the protected stage (with Boc groups on the side chain nitrogens) were analyzed by gel permeation chromatography (GPC) using THF as the mobile phase. Side chain groups of polymers were deprotected using neat trifluoroacetic acid (TFA) with 5% (v/v) of triisopropylsilane (TIPS) relative to TFA. The deprotected copolymers were characterized by proton nuclear magnetic resonance ( $^1\text{H}$  NMR) spectroscopy.

Proton ( $^1\text{H}$ ) Nuclear Magnetic Resonance (NMR) spectra for all polymers were obtained on a Bruker Avance III spectrometer at 500 MHz. All proton chemical shifts are reported in ppm using the solvent as the internal standard ( $\text{D}_2\text{O}$  at 4.790 ppm). Gel permeation chromatography (GPC) analysis, with THF as eluent, involved two involved two Waters columns (Styragel HR 4E and HR 2 particle size 5  $\mu\text{m}$ ) linked in series. The Waters liquid chromatography unit (Alliance) was equipped with a multiangle light scattering detector (Wyatt miniDAWN TREOS, 658 nm) and a refractive index detector (Wyatt Optilab-rEX, 658 nm). The number average molecular weight ( $M_n$ ) and dispersity ( $\mathcal{D}$ ) of polymers included in Table S1 were calculated using ASTRA software with a  $dn/dc$  value of 0.1 mL/g.

## Cell growth and preparation for imaging

Bulk cultures were grown in EZ rich, defined medium (EZRDM), which is a morpholinepropanesulfonic acid (MOPS)-buffered solution at pH = 7.4 supplemented with metal ions (M2130; Teknova), glucose (2 mg/mL), amino acids and vitamins (M2104; Teknova), nitrogenous bases (M2103; Teknova), 1.32 mM K<sub>2</sub>HPO<sub>4</sub>, and 76 mM NaCl. Cultures were grown from glycerol frozen stock to stationary phase overnight at 30°C. Subcultures were grown to exponential phase (OD = 0.2–0.6 at 600 nm) at 30°C before sampling for the microscopy experiments.

Strains used in the study and the corresponding MIC are summarized in Tables 1, S1, and S2. Strains that express labeled species from a plasmid are grown with addition of 100 µg/mL ampicillin. When the cells reach mid-log phase, anhydrotetracycline was added to a final concentration of 45 nM to induce the expression of the labeled protein of interest. After 10 min of induction, the cells were centrifuged and resuspended in fresh growth media with 100 µg/mL ampicillin to remove the inducer. The cells were then incubated again in growth media for 15 min at 30°C to enable maturation of the labeled protein of interest prior to imaging. For studying cells under ATP-depleting conditions, cells were treated with 200 µM carbonylcyanide-*m*-chlorophenylhydrazone (CCCP) plus 1 mM 2-deoxyglucose (8-13). These were added to the subcultures for 10 min prior to imaging. During the imaging, EZRDM was supplemented with each drug at the same concentration.

Two different imaging methodologies were employed, a flow chamber and a static chamber. Single-cell, time-lapse imaging experiments on the ribosome S2-YFP, ppGFP, nucleoid stained by Sytox Orange (S11368, Thermo-Fisher Scientific) and DNA locus *Right2* were carried out at 30°C in a PDMS-based microfluidics chamber consisting of a single rectilinear channel of uniform height of 50 µm, width of 6 mm and length of 11 mm. The total

chamber volume is ~10  $\mu\text{L}$ . After attachment of the PDMS chamber to the glass coverslip, 10  $\mu\text{L}$  of 0.01% poly-L-lysine (molecular weight >150,000 Da) was flowed through the chamber and allowed to adsorb for 30 min. The chamber was then rinsed thoroughly with ultrapure water to remove excess poly-L-lysine. When the subcultures had grown to midlog phase, we flowed culture containing *E. coli* cells through the microfluidic chamber, followed by fresh, aerated, warmed EZRDM to wash away any unbound cells. The remaining cells are immobilized on the coverslip but grow normally. The PDMS ceiling of the microfluidics device is permeable to the ambient gases  $\text{N}_2$  and  $\text{O}_2$ . The microfluidics chamber allows flowing of appropriate chemicals necessary for the experiment such as polymer solution or Sytox Orange during imaging.

Single-molecule imaging of ribosomes S2-mEos2, ribosome S2-Dendra2 and HU-PAmCherry was carried out in a static chamber. First, ~150  $\mu\text{L}$  of cell culture was placed within a CoverWell perfusion chamber gasket (Invitrogen) on a poly-L-lysine -coated, cleaned coverslip to fill the entire chamber volume. We allowed 2 min for the cells to adhere to the coverslip. The plated cells were then rinsed with the appropriate fresh, warmed, aerated media to wash away any non-adhered cells. For imaging of cells under normal growth conditions, the rinsing medium is EZRDM. Cells continue to grow normally for at least 30 min under these conditions. For AMP or polymer treated conditions, the rinsing medium is AMP or polymer in EZRDM solution. The cells are grown in the corresponding medium and maintained at 30°C throughout the imaging using an automatic temperature controller.

For nucleoid staining experiments, Sytox Orange dye was added to a growing mid-log-phase culture (OD = 0.2–0.6 at 600 nm) to a final concentration of 500 nM (14). After 10 min of incubation, the cells were centrifuged twice and resuspended in fresh EZRDM before imaging. The rinsing steps eliminate background fluorescence from dye molecules that adhere to the coverslip without removing Sytox Orange from the cytoplasm.

## Microscopy

All imaging was performed on a Nikon Eclipse Ti inverted microscope (Nikon) with an oil immersion 100 $\times$ , 1.45 N.A. phase contrast objective (CFI Plan Apo Lambda DM; Nikon Instrument). The images were further magnified 1.5 $\times$ . Fast shutters (Uniblitz LS2; Vincent Associates) were used to synchronize illumination and image acquisition. Images were recorded by a back-illuminated EMCCD camera with 16  $\mu\text{m} \times 16 \mu\text{m}$  pixels (either Andor iXon DV-897 or Andor iXon DV-887; Andor Technology). Each pixel corresponds to 105  $\times$  105 nm<sup>2</sup> at the sample with an overall magnification of 150 $\times$ .

Studies of the motion of the DNA loci *Right2* labeled by ParB-GFP (strain JCW154) were imaged using 488 nm excitation (Coherent Sapphire laser), expanded to illuminate the field of view uniformly. The laser intensity was  $\sim 100 \text{ W/cm}^2$  at the sample plane. The emission filter was HQ525/50 (Chroma Technology). The labeled ParB-GFP protein polymerizes specifically at a *parS* site engineered into the chromosome near the locus *Right 2*, forming bright puncta. The loci could be tracked with good signal-to-noise for 600 camera frames at 1s/frame and 50 ms exposure time.

For experiments with dual color imaging of ppGFP (green channel) and Sytox Orange (red channel),  $\mu$ Manager was used to obtain the data and switch filters between frames using a LB10-NW filter wheel (Sutter). The time-lapse videos were obtained as 50 ms exposure time each, with green fluorescence (488 nm excitation), red fluorescence (561 nm excitation), and phase contrast images interleaved (12 s per complete cycle). To minimize spectral bleed-through in the two-color experiments, we utilized the narrower filters HQ510/20 for the green channel and HQ600/50M for the red channel. Laser intensities at the sample were typically  $\sim 5 \text{ W/cm}^2$  at 488 nm and  $\sim 2.5 \text{ W/cm}^2$  at 561 nm. For dual color experiments imaging ribosome S2-YFP



(green channel) and Sytox Orange (red channel), the same microscopic parameters were applied except 1 min per imaging cycle.

For super-resolution imaging of HU-PAmCherry (strain SM7), ribosomes labeled by S2-mEos2 (strain MDG196) and S2-Dendra2, the fluorescent protein was photoconverted using a 405 nm laser at  $\sim 4\text{-}12\text{ W/cm}^2$  and subsequently imaged using a 561 nm excitation laser at  $\sim 2\text{ kW/cm}^2$ . The emission filter was ET610/75 (Chroma Technology). HU-PAmCherry, ribosome S2-mEos2 and ribosome S2-Dendra2 were imaged at a frame rate of 31.2 Hz, with an exposure time of 30 ms.

### **Minimum Inhibitory Concentration (MIC) Assay**

The MIC value for the AMPs and polymers were determined using the broth microdilution method as previously described (8). Two-fold serial dilutions of drug in  $1\times$  EZRDM were performed in separate rows of a polystyrene 96-well plate, with each plate containing an inoculum of *E. coli*. The inoculum was a 1:20 dilution from a bulk culture at midlog phase ( $\text{OD}_{600} = 0.5$ ) grown at  $30^\circ\text{C}$ . The plate was incubated at  $30^\circ\text{C}$  and shaken at 200 rpm in a Lab-Line Orbital Environ Shaker (Model 3527) for 6 hr. The MIC value was taken as the lowest concentration for which no growth was discernible ( $<0.05\text{ OD}$ ) after 6 hr.

### **Data analysis**

Images were analyzed using a MATLAB graphical user interface (GUI) developed in our lab (15). Images were smoothed and filtered to obtain a zero-based image. Bright spots were located with pixel-level accuracy by a peak finding algorithm that detects the local intensity maxima within an image. A user defined intensity threshold was used as the minimum brightness of a pixel arising from a single molecule. The threshold is carefully set by the user so that it will not be so high as to reject a real single molecule in the raw images or so low as to include background noise.

A modified MATLAB version of the tracking program written by Crocker and Grier (16) was used. As before (4), a centroid algorithm was used to locate the identified particles with subpixel resolution. Centroids of the bright spots were calculated from a 7 x 7 pixel square containing the entire bright spot, centered on the local maximum determined by the peak finding algorithm. The centroid positions from successive frames were connected to form a trajectory. In each experimental condition, the ensemble-averaged mean-square displacement was calculated as:

$$MSD(\tau) = \langle (\vec{R}(t + \tau) - \vec{R}(t))^2 \rangle = \frac{1}{N} \sum_i \frac{1}{m} \sum_m [\vec{R}_i(mt + \tau) - \vec{R}_i(mt)]^2$$

Here  $N$  is the number of trajectories over which the ensemble average is taken. The index  $m$  runs from 1 to a specific value given the lag time  $\tau$ , providing the time average of each trajectory. The final MSD is an average over the ensemble and over time. For DNA loci imaged with 1 s/frame time,  $m$  runs from 1 to 99. We used the linear fit of the first 10 points on the MSD plots to calculate an approximate apparent diffusion coefficient. For ribosomal S2-mEos2, ribosomal S2-Dendra2 and HU-PAmCherry,  $m$  runs from 1 to 6 and we used the linear fit of the first 3 points on the MSD plots to calculate an approximate apparent diffusion coefficient via an average over thousands of trajectories (17).

Suppose the least-squares, best fit to the first 10 or 3 experimental points of a mean-square displacement plot is given by the equation  $MSD(\tau) = a + b\tau$ , with  $b$  the slope and  $a$  the extrapolated intercept at lag time  $\tau = 0$ . Then Michalet (17) has shown that the most accurate mean diffusion coefficient is given by  $D = b/4$  and the best estimate of the dynamic localization error is  $\sigma = \frac{1}{2} (a + 4Dt_E/3)^{1/2}$ , where  $t_E$  is the exposure time per camera frame. Mean diffusion coefficients of different species in the various experiment of conditions are collected in Tables 4.

In the HU super-resolution distribution section, to obtain the tip-to-tip cell length and to define the  $(x,y)$  coordinates of each particle within the cell, cell outlines were generated from

phase contrast images by the open-source image analysis software Oufi (18). To generate the spatial distribution of HU molecules, the camera based coordinates are reoriented so that the  $x$  axis and  $y$  axis correspond to the long and short principle cell axes.

### **Continued segregation of DNA and ribosomes after MM-CH treatment**

In normally growing *E. coli* cells, the DNA and the ribosomal species are strongly segregated from each other. Ribosome-DNA exclusion plays an important role in shaping DNA morphology (19,20). To explore the spatial distributions of DNA and ribosomes after MM-CH treatment, we stained the DNA of bacteria strain MSG192 (Table S2) with Sytox Orange as above. In this strain, the ribosomal S2 protein is labeled with YFP. S2 resides on the surface of the 30S ribosomal subunit. As before, we flowed  $2\times$  MIC MM-CH beginning at  $t = 0$ . Images of phase contrast, Sytox Orange, and ribosome S2-YFP were interleaved at an overall cycle time of 1 min per frame. A representative bacterial cell is shown in Fig. S3A and Video S2. As before (19,20), in normal growth conditions prior to the addition of MM-CH, ribosomes are concentrated axially in the endcaps and at the cell center and radially in the thin annular region surrounding each nucleoid lobe. DNA remains in the nucleoid region and shows two axial peaks. There is a strong anticorrelation between the spatial distributions of DNA and the ribosomes (Fig. S3A, B).

At  $t \sim 40$  min, the left nucleoid lobe has largely merged with the right lobe (Fig. S3A-C). At the same time, much of the ribosome distribution has moved to the left side of the cell, where the DNA has become sparse. The strong anticorrelation of DNA and ribosome distributions persists. Interestingly, the phase contrast image shows a white band that grows in where the ribosomes accumulate but DNA is depleted. This is a region of relatively low refractive index. Even at  $t = 90$  min, when the left nucleoid lobe has partially recovered, the ribosomes still preferentially locate in the left side of the cell. Evidently the right nucleoid lobe remains dense

enough to exclude the ribosomes even at a very late stage. Out of 23 observed cells, 16 showed DNA and ribosome morphological changes similar to those described above.

### **Upper Bound on Amount of charge on MM-CH absorbed per cell**

The method to quantify the absorbed MM-CH is based on that described previously by the Wimley lab (21). We applied this method to determine the amount of MM-CH and charges absorbed per cell for the lowest concentration of MM-CH that kills all the cells in the sample.

We first prepared combinations of different concentrations of MM-CH and different initial cell counts to determine the number of MM-CH molecules needed to kill the bacteria at different cell counts. We grew cells to OD = 1.0 or higher in EZRDM, then centrifuged and resuspended the cells in 1× PBS. After that we determine the CFU in each sample by measurement of OD600 and the scaling equation  $OD\ 1.0 = 1.5 \times 10^8\ \text{CFU/mL}$ . Serial dilution using 1× PBS then provided a range of initial cell counts. We incubated each specific number of cells with various specific concentrations of MM-CH in the test tube in PBS solution for 60 min at 30°C. After that we added 50  $\mu\text{L}$  solution from each tube (each particular combination of cell number and MM-CH concentration) to polystyrene 96-well plates supplemented with 50  $\mu\text{L}$  2× EZRDM in each well. We measured the OD595 ( $OD_{t=0}$ ), incubated 24 h, and measured the OD 595 again ( $OD_{t=24\ \text{h}}$ ). Thus, we could determine the 24 h OD increase ( $\Delta OD = OD_{t=24\ \text{h}} - OD_{t=0}$ ) for each particular combination (Fig. S6). If the OD does not increase significantly after 24 h, then the initial MM-CH concentration was sufficient to kill that initial number of cells. In this way we can set the minimum bulk MM-CH concentration which is required to kill a particular initial number of cells.

For example, we found 25  $\mu\text{g/mL}$  MM-CH can completely kill bacteria with initial count of  $9 \times 10^6$  CFU/mL, but not a higher initial count. The ratio of total MM-CH copies to the initial number of cells provides an upper bound on the number of copies absorbed per cell. The

combination of 25  $\mu\text{g}/\text{mL}$  MM-CH and  $9 \times 10^6$  CFU/mL yields an upper bound of  $\sim 2.8 \times 10^{-6}$   $\mu\text{g}$  MM-CH absorbed per cell. Since there is a distribution of polymer chain length, we cannot directly calculate number of polymers per bacterial cell. However, the ratio of cationic subunit MM and hydrophobic subunit CH is fixed, in our case MM: CH = 64.8 % : 35.2%.

Suppose A = MM subunit, with charge +1 , molecular weight  $M_A = 228.7$  g/mol and mol fraction of A =  $n_A = 64.8\%$ ; Suppose B = CH subunit, with charge 0, molecular weight  $M_B = 125.17$  g/mol and mol fraction of B =  $n_B = 35.2\%$ ; The degree of polymerization  $N = 32$  determined by NMR. We can calculate

$$\text{weight fraction of A : } w_A = \frac{M_A \times n_A}{M_A \times n_A + M_B \times n_B} = 77.8\%$$

$$\text{weight fraction of B : } w_B = \frac{M_B \times n_B}{M_A \times n_A + M_B \times n_B} = 22.2\%$$

And the number of total charges in 1 mL solution is :

$$\frac{25 \mu\text{g}/\text{mL} \times 77.8\% \times 1\text{mL}}{228.17 \text{ g/mol}} = 5.13 \times 10^{16}$$

Then number of total charges per cell is:

$$\frac{25 \mu\text{g}/\text{mL} \times 77.8\%}{228.17 \text{ g/mol} \times 9 \times 10^6 \text{ CFU/mL}} = 5.7 \times 10^9$$

Similar calculation can be applied for MM-CH concentration of 50  $\mu\text{g}/\text{mL}$ , whose critical initial cell concentration occurred at  $4 \times 10^7$  CFU/ml. The number of charges per cell is  $\sim 2.6 \times 10^9$ . Of course, the conditions in these MM-CH uptake experiments are quite different from those in the microscopy experiments. The uptake experiments are carried out in PBS to avoid interference in the absorption measurements by the multitude of species present in EZRDM. In addition, in the microscopy experiments the flow of a constant concentration of MM-CH provides an unlimited source of peptide after membrane permeabilization has occurred. And not all the MM-CH enters the cell and the cytoplasm. Nevertheless, we view  $\sim 10^9$  positive charge absorbed per cell as a sensible first estimate. The average degree of polymerization determined

by NMR is  $N=32$ ; The polydispersity  $M_w/M_n$  is 1.07 determined from GPC (Table S1), and this indicates a narrow chain length distribution. Therefore, most of charges are on the polymer longer than 30 units.

Under our growth conditions the  $\sim 2.3$  chromosomes carry  $\sim 2.1 \times 10^7$  negative phosphate charges, compensated by cytoplasmic counterions such as  $K^+$  (22). The  $\sim 50,000$  ribosomes, each with charge of  $-4500$ , bring a total of  $\sim 2.2 \times 10^8$  negative charges (4). Half of these charges are compensated by ribosomal proteins and structural  $Mg^{2+}$  cations (22). The  $\sim 375,000$  tRNA copies carry  $\sim 80$  phosphates each for a total of  $\sim 3 \times 10^7$  negative charges (23). The mRNA contributes more or less the same as tRNA (24). These cytoplasmic species alone provide  $\sim 2 \times 10^8$  negative charges ( $\sim 200$  mM) residing in cytoplasmic polyanionic species that are compensated primarily by  $K^+$ .

### **Spatial distribution of DNA revealed by super-resolution imaging of HU**

To confirm the results obtained from single-cell, widefield imaging, we study the DNA distribution by super-resolution microscopy using a strain SM7, which expresses HU- PAmCherry from a plasmid after induction. HU dimer is a nucleoid-associated protein that binds nonspecifically to the chromosomal DNA. We have shown before that the distribution of HU is a good proxy for the chromosomal DNA distribution, as judged by its comparison with Sytox Orange (20). The images were taken at 30 ms per frame.

We first obtained the composite distribution of HU averaged across cells in a narrow cell length range of  $4-4.3 \mu\text{m}$  determined from the tip-to-tip length in phase contrast images. We projected this distribution onto the cell long axis to form the axial 1D distributions  $P(x)$  and onto the cell short axis to form the radial distribution  $P(y)$  (Fig. S4A). Radial distribution includes only molecules in the nucleoid region ( $0.4 \mu\text{m} < |x| < 1.2 \mu\text{m}$ ). The composite distribution averaged across different cells look similar for normal cells and cells after the polymer treatment (Fig. S4A). However, there is more heterogeneity

among the cells after polymer and results in a more irregular composite axial distribution. The overall HU radial distribution is also slightly narrower for cells after polymer.

The heterogeneity is more obvious when we look at the single cell HU distribution. We found cells after MM-CH which have enough detected HU molecules per cell to exhibit a clear pattern can be classified into two categories. The first type of cells has the usual symmetric distribution of HU, as shown in Fig. S4B. The other category has an asymmetric distribution of HU, i.e. HU was distributed mostly at one end of the cell. It could either be the case where all the HU molecules are in one side of the cell or the case where there are molecules on both sides, but one side has too few molecules so that the axial peak ratio is greater than 5:1 (Fig. S4C).

For cells after MM-CH in the length range of 4–4.3  $\mu\text{m}$ , we have 17 cells showing symmetric distribution of HU; 22 cells showing asymmetric distribution of HU. For cells after MM-CH in the length range of 3.5–4  $\mu\text{m}$ , we have 46 cells exhibiting symmetric distribution of HU; 43 cells showing asymmetric distribution of HU. In contrast, for cells in normal growth condition in the length range of 4–4.3  $\mu\text{m}$ , there is 52 cells showing normal symmetric two-lobe distribution while only 2 cells exhibiting asymmetric distribution. Therefore, the large fraction of cells with asymmetric HU after MM-CH is not caused by random probability but due to the effect of MM-CH.

We next compared the single cell nucleoid radius of cells without treatment and cells 25 min after MM-CH and with two nucleoid lobes. We determined the single cell nucleoid radius by fitting the HU radial distribution  $P(y)$  to a simulated distribution for a uniformly filled spherocylinder with various radius to find the best fit. The nucleoid radius distribution are shown in Fig S5.

## Supporting References

1. Espeli, O., R. Mercier, and F. Boccard. 2008. DNA dynamics vary according to macrodomain topography in the *E. coli* chromosome. *Mol. Microbiol.* 68(6):1418-1427, doi: 10.1111/j.1365-2958.2008.06239.x.
2. Sochacki, K. A., I. A. Shkel, M. T. Record, and J. C. Weisshaar. 2011. Protein Diffusion in the Periplasm of *E. coli* under Osmotic Stress. *Biophys. J.* 100(1):22-31.
3. Bakshi, S., H. Choi, J. Mondal, and J. C. Weisshaar. 2014. Time-dependent effects of transcription- and translation-halting drugs on the spatial distributions of the *Escherichia coli* chromosome and ribosomes. *Mol. Microbiol.* 94(4):871-887, doi: 10.1111/mmi.12805.
4. Bakshi, S., A. Siryaporn, M. Goulian, and J. C. Weisshaar. 2012. Superresolution imaging of ribosomes and RNA polymerase in live *Escherichia coli* cells. *Mol. Microbiol.* 85(1):21-38, doi: 10.1111/j.1365-2958.2012.08081.x.
5. Mohapatra, S., and J. C. Weisshaar. 2018. Functional mapping of the *E. coli* translational machinery using single-molecule tracking. *Mol. Microbiol.* 110:262-282, doi: 10.1111/mmi.14103.
6. English, B. P., V. Hauryliuk, A. Sanamrad, S. Tankov, N. H. Dekker, and J. Elf. 2011. Single-molecule investigations of the stringent response machinery in living bacterial cells. *Proc. Natl. Acad. Sci. U.S.A.* 108(31):E365-E373.
7. Mowery, B. P., A. H. Lindner, B. Weisblum, S. S. Stahl, and S. H. Gellman. 2009. Structure-activity Relationships among Random Nylon-3 Copolymers That Mimic Antibacterial Host-Defense Peptides. *J. Am. Chem. Soc.* 131(28):9735-9745.
8. Choi, H., Z. Yang, and J. C. Weisshaar. 2015. Single-cell, real-time detection of oxidative stress induced in *Escherichia coli* by the antimicrobial peptide CM15. *Proc. Natl. Acad. Sci. U. S. A.* 112(3):E303-310, doi: 10.1073/pnas.1417703112.
9. Stannard, J. N., and B. L. Horecker. 1947. The *In vitro* Inhibition of Cytochrome Oxidase by Azide and Cyanide. *Fed. Proc.* 6(1):210-210.
10. Weber, S. C., A. J. Spakowitz, and J. A. Theriot. 2012. Nonthermal ATP-dependent fluctuations contribute to the in vivo motion of chromosomal loci. *Proc. Natl. Acad. Sci. U. S. A.* 109(19):7338-7343, doi: 10.1073/pnas.1119505109.
11. Cavari, B. Z., Y. Avidor, and Grossowil. 1967. Effect of Carbonyl Cyanide M-Chlorophenylhydrazone on Respiration and Respiration-Dependent Phosphorylation in *Escherichia coli*. *Biochem. J.* 103(2):601-&.
12. Weber, S. C., A. J. Spakowitz, and J. A. Theriot. 2010. Bacterial chromosomal loci move subdiffusively through a viscoelastic cytoplasm. *Phys. Rev. Lett.* 104(23):238102, doi: 10.1103/PhysRevLett.104.238102.
13. Kralj, J. M., D. R. Hochbaum, A. D. Douglass, and A. E. Cohen. 2011. Electrical Spiking in *Escherichia coli* Probed with a Fluorescent Voltage-Indicating Protein. *Science.* 333(6040):345-348.
14. Bakshi, S., H. Choi, N. Rangarajan, K. J. Barns, B. P. Bratton, and J. C. Weisshaar. 2014. Nonperturbative imaging of nucleoid morphology in live bacterial cells during an antimicrobial peptide attack. *Appl. Environ. Microbiol.* 80(16):4977-4986, doi: 10.1128/AEM.00989-14.



15. Bakshi, S., B. P. Bratton, and J. C. Weisshaar. 2011. Subdiffraction-limit study of Kaede diffusion and spatial distribution in live *Escherichia coli*. *Biophys. J.* 101(10):2535-2544, doi: 10.1016/j.bpj.2011.10.013.
16. Crocker, J. C., and D. G. Grier. 1996. Methods of Digital Video Microscopy for Colloidal Studies. *J. Colloid Interface Sci.* 179(1):298-310, doi: <https://doi.org/10.1006/jcis.1996.0217>.
17. Michalet, X. 2010. Mean square displacement analysis of single-particle trajectories with localization error: Brownian motion in an isotropic medium. *Phys. Rev. E Stat. Nonlin. Soft Matter Phys.* 82(4 Pt 1):041914, doi: 10.1103/PhysRevE.82.041914.
18. Paintdakhi, A., B. Parry, M. Campos, I. Irnov, J. Elf, I. Surovtsev, and C. Jacobs-Wagner. 2016. Oufiti: an integrated software package for high-accuracy, high-throughput quantitative microscopy analysis. *Mol. Microbiol.* 99(4):767-777.
19. Bakshi, S., H. Choi, and J. C. Weisshaar. 2015. The spatial biology of transcription and translation in rapidly growing *Escherichia coli*. *Front. Microbiol.* 6:636, doi: 10.3389/fmicb.2015.00636.
20. Mohapatra, S., and J. C. Weisshaar. 2018. Functional mapping of the *E. coli* translational machinery using single-molecule tracking. *Mol. Microbiol.*, doi: 10.1111/mmi.14103.
21. Starr, C. G., J. He, and W. C. Wimley. 2016. Host Cell Interactions Are a Significant Barrier to the Clinical Utility of Peptide Antibiotics. *ACS Chem. Biol.* 11(12):3391-3399, doi: 10.1021/acscchembio.6b00843.
22. Record, M. T., Jr., E. S. Courtenay, D. S. Cayley, and H. J. Guttman. 1998. Responses of *E. coli* to osmotic stress: large changes in amounts of cytoplasmic solutes and water. *Trends Biochem. Sci.* 23(4):143-148.
23. Dong, H., L. Nilsson, and C. G. Kurland. 1996. Co-variation of tRNA abundance and codon usage in *Escherichia coli* at different growth rates. *J. Mol. Biol.* 260(5):649-663, doi: 10.1006/jmbi.1996.0428.
24. Joyeux, M. 2016. In vivo compaction dynamics of bacterial DNA: A fingerprint of DNA/RNA demixing? *Current Opinion in Colloid & Interface Science.* 26:17-27.